NUMERICAL INVESTIGATION OF HEAT TRANSFER AND CONTROL OF VORTEX SHEDDING IN THE WAKE OF A CIRCULAR CYLINDER

by

VEERABATHRASWAMY K.

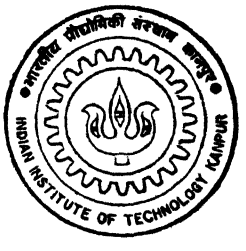

DEPARTMENT OF MECHANICAL ENGINEERING

INDIAN INSTITUTE OF TECHNOLOGY KANPUR

May, 1997

NUMERICAL INVESTIGATION OF HEAT TRANSFER AND CONTROL OF VORTEX SHEDDING IN THE WAKE OF A CIRCULAR CYLINDER

A Thesis Submitted

in Partial Fulfillment of the Requirements

for the Degree of

MASTER OF TECHNOLOGY

by

VEERABATHRASWAMY K.

to the

DEPARTMENT OF MECHANICAL ENGINEERING
INDIAN INSTITUTE OF TECHNOLOGY KANPUR

May, 1997

CERTIFICATE

It is certified that the work contained in the thesis entitled "*Numerical Investigation of Heat Transfer and Control of Vortex Shedding in the Wake of a Circular Cylinder*", by *Veerabathraswamy K.*, has been carried out under our supervision and that this work has not been submitted elsewhere for a degree.

(On leave)
Gautam Biswas
Professor
Department of Mechanical Engineering
I.I.T , Kanpur

Kartik Venkatraman
Visiting Faculty
Department of Mechanical Engineering
I.I.T., Kanpur

May, 1997.

ACKNOWLEDGEMENT

I express my sincere gratitude to my thesis supervisors **Dr. Gautam Biswas** and **Dr. Kartik Venkatraman** for their guidance and support throughout the course work. I owe the greatest debt to them. The time I spent with them is the most fruitful and potential learning period of my life. I am very grateful to their friendly and encouraging nature.

I am deeply indebted to the research scholars in the CFD Lab for their valuable suggestions and help time to time.

Thanks are also due to my classmates and Tamil friends for making my stay at IIT Kanpur a memorable one.

Veerabathraswamy k.

Contents

List of Figures

Nomenclature

A	Area of the control volume
C	A parameter, $Re_d \cdot C_f$
C_f	Skin friction coefficient, $\frac{2\mu\frac{\partial u}{\partial y}}{(\rho U_{ave}^2)}$
D	diameter of the cylinder
f	Frequency of vortex shedding
Gr	Grashof number, $\beta\, g(T_w - T_{in})D^3/\nu^2$
H	Channel height
J	Jacobian of geometry transformation
L	Length of the channel
l	Length of the control volume face
M	Shape function for pressure variables
n_x , n_y	Direction cosines of outward unit normal on control volume faces
N	Shape functions for velocity variables
Nu_l	Local Nusselt number, $\frac{\partial\theta}{\partial y}$
p	Pressure
P	Non-dimensional pressure, $\frac{p}{\rho U_a^2 v}$
Pe	Peclet number (Re Pr)
Re	Reynolds number based on the cylinder diameter, $\frac{U_{ave}D}{\nu}$
Ri	Richardson number, Gr/Re^2
St	Strouhal number, $\frac{f\ D}{U_{ave}}$
τ	Non-dimensional time, $t/\ (H/U_{ave})$
t	time
u	Axial velocity component

v	Normal velocity component
U	Non-dimensional axial velocity component, u/U_{ave}
V	Non-dimensional normal velocity component, v/U_{ave}
x	Axial dimension of the coordinates
X	x/H
y	Normal dimension of the coordinates
Y	y/H

Greek letters

α	Upwinding factor
μ	Dynamic viscosity of the fluid
ν	Kinematic viscosity of the fluid
ρ	Density of the fluid
θ	Nondimensional Temperature $(T - T_{\text{inf}})/(T_w - T_{\text{inf}})$
ξ, η	Coordinates in the computational space

Subscripts

ave	Average
CS1	Bouandary of the continuity control volume
CS2	Bouandary of the momentum control volume
CV1	Continuity control volume
CV2	Momentum control volume
n, (n+1)	timelevel
w	wall

Chapter 1

Introduction

1.1 General Introduction

Knowledge of heat transfer and fluid flow is essential for effective design of engineering equipment, studying the natural environment, and the biological changes within the living body. Prediction of the flow physics is possible both by experimental and theoretical investigations, of which experimental methods are the most reliable. Time, and the total cost involved in conducting the experiments, and the practical difficulties contained therein, necessitates carrying out theoretical investigations. Prediction by theoretical means may by broadly classified as analytical and numerical methods. Analytical methods have the distinct advantage of immediately highlighting some of the flow physics. However, real life situations are so complicated that analytical solutions are not possible for most of the cases. Recent developments in numerical methods, and the easy availability of powerful computers enables the numerical simulation of complex, realistic systems. Aerospace research, combustion studies, design of heat exchangers, and meteorological predictions, are some of the important areas where these computational methods play a vital role. Using sophisticated numerical methods, it is possible to model the flow involving fast transients, high temperature conditions, and involving toxic substances, which may not be possible by experimental means.

1.2 Literature Review

1.2.1 Solution Algorithm

Any model related to flow and heat transfer problems, deals with the Navier- Stokes and energy equations in various forms. The nonlinearity in the convective terms of these equations and the absence of a equation for pressure, presents a challenge for determining the solution for these equations. Finite difference formulation, finite element methods, and control volume formulation are some of the procedures used to solve these equations. Of all these, finite difference scheme is the basic and easier method to develop with orthogonal grids. Explicit difference methods like MAC (Marker and Cell) of Harlaw and Weich (1965) and SMAC (Simplified MAC) of Harlaw and Amsden (1970) are well known. In these algorithms, the provisional velocities at any time step are estimated from momentum equations using the velocities and pressure of the earlier time step. These computed velocities when used in the continuity equations may give non-zero mass accumulation which is physically incorrect. This divergence is used in turn to correct the pressure and velocity which gives a Poisson type equation for pressure. This equation is solved iteratively to get the correct velocity and pressure fields. However, this explicit method has a restriction on time step, which comes from the stability conditions. Implicit difference methods like SIMPLE (Semi Implicit Method for Pressure Linked Equations) and SIMPLER (SIMPLE Revised) of Patankar (1978,1981) overcomes this restriction. But the development of orthogonal grids is not always possible because of complex geometries which gives constraints in applying finite difference schemes. Finite element formulation which appears to be a viable alternative for complex flow situations, also have some drawbacks like lack of transportive properties in the diffusion terms. The most suited and versatile method is control volume formulation in which all the above difficulties are removed.

Despite the development of many algorithms for complex incompressible flow simula-

tions, the algorithm developed by Mukhopadhyay *et al*(1993) has the advantage of using the powerful tool of finite element method (FEM) in control volume formulation. This algorithm is used and extended for solving coupled energy equation and is explained in detail in the next chapter.

1.2.2 Flow Past Circular Cylinder

Use of circular pipes in heat exchangers necessitates the understanding of flow physics over a circular cylinder. Because of large pressure gradient caused by cylinder geometry, the main flow gets separated. If the Reynolds number of flow becomes larger than critical Reynolds number($Re_c \sim 40$) vortex asymmetry results. Loss of energy, increase in pressure drag, periodic force in normal direction etc., are some of the effects of separation with asymmetry.

When there is temperature difference between the flowing fluid and the cylinder, the thermal buoyancy force which results in flow in the vertical direction, against the gravitational force is of importance. Its effect and significance over the flow properties have been studied by many researchers. Patankar *et al*(1978) showed that combined convection in a horizontal tube with bottom heating results in a vigorous buoyancy induced flow, and as a result the average Nusselt number become much higher than that for pure forced convection. They have also reported a flow transition from a two-vortex pattern to four-vortex pattern above a Grashof number of 10^5. Incropera and Schutt(1985) and Incropera *et al*(1987) showed that manifesting its effect on velocity and temperature field, buoyancy can enhance heat transfer, alter the entry length, and induce transition to turbulence.

In the case of vertical flow, the velocity induced by the free convection will be either aligned or opposed to that of the forced convection. It is observed by many researchers, in comparison to pure convection, that in the case of buoyancy induced convection (aligned

with forced convection), the wake region is diminished and the separation points are shifted down stream. But when the buoyancy is opposed to the forced convection, the size of the wake is increased and the separation is advanced. These change in flow characteristics significantly changes the heat transfer characteristics.

When the flow is in the horizontal channel, the effect of mixed convection makes the physics highly complex and it behaves entirely different from that in a vertical channel. The velocity induced by the thermal buoyancy will be normal to the forced flow direction and will distort the vortex shedding in the wake of the bluff body. The fluid will move up from the bottom wall to the top wall and will return back, creating any number of separated zones and eddies, depending on the relative magnitude of the Reynolds number and Grashof number. These wall eddies will interact with the vortex street. If the channel wall and the surface of the cylinder have higher temperatures than the incoming flow, one would, at first, expect flow separation as a result of the plume building at the bottom wall. However, further investigation indicates that the fluid particles will rise from bottom to the top and turn around at the upper wall, causing flow separation. Mass conservation then dictates an increased fluid velocity near the bottom wall.

In mixed convection flows, one would normally expect enhancement of heat transfer between the fluid and the surfaces over the corresponding pure forced convection flows. However, flow separation will hinder this enhancement. Again the relative magnitude of Re and Gr will decide whether free convection has beneficial or adverse effects on heat transfer. G. Biswas *et al*(1990) considered mixed convection from a square cylinder placed in a horizontal channel and reported change of heat transfer rate and skin friction coefficient. He also noted that mixed convection causes a movement of maxima of velocity profiles and minima of temperature profiles closer to the bottom wall, perturbation of the steady wake at the rear of the obstacle, and a transition to periodic flow.

1.2.3 Control of Vortex Shedding

Increase in drag force on the cylinder and periodic force in the normal direction to the main stream are some of the effect of vortex shedding. With increase in vortex shedding these forces increase which consequently shorten the life of the structure. On the other hand, vortex shedding enhances mixing behind the cylinder which in turn increases heat transfer. This increase in heat transfer is favourable in some cases. Therefore, controlling the vortex shedding is very useful in practical situations.

Theoretical studies using linear stability analysis have shed new light on the local absolute /convective nature of wake flow instabilities, which gives a new frame of understanding the vortex street formation and its evolution. Numerical studies of these wake flow evolving in both space and time extend these theoretical studies to practical cases. Among the bluff bodies, circular cylinder has received considerable attention not only because of geometric simplicity but also because of its practical importance.

Controlling of vortex shedding can be achieved by either passive or active methods. Splitter plate, base bleed, periodic rotation of the cylinder, heating and cooling of the walls, inclusion of acoustic source in the flow field, wall motion, and the use of small cylinders in the wake region are some of successful methods to mention. P. J. Strykowski and K. R. Srinivasan(1990) studied the effect of having a small cylinder in the wake. The have reported a control region within which if the control cylinder is placed, vortex shedding can be completely suppressed This control region changes with Reynolds number and the diameter ratio of the cylinders. However, this control method cannot be used if Reynolds number is more than 120.

A. Ongoven and D. Rockwell(1988) reported the effect of oscillation of the cylinder on the vortex street. When the oscillation frequency is equal to the shedding frequency, there is substantial reduction in the vortex formulation and the length of vortex street. Suction and blow of fluid in the wake region also helps in controlling the vortex genera-

tion. Gunzburger and Lee(1996) have showed the effect of suction and blowing on the flow field. Using pressure sensors in the flow field and a simple feedback law, they achieved the reduction in the oscillation in the lift coefficient. But the feed back law is not optimal.

By heating or cooling the walls we can increase or decrease the viscosity of the fluid which influences the separation and hence shedding of vortices. The effect of wall heating is studied for flow over flat plate by many researchers. For larger Prandtl number flows, the effect of heating is more due to good thermal coupling. It is possible to delay the transition with only few degrees change in temperature. The work of Frick and McCullough(1942) and Liepmann and Fila(1947) are noteworthy contribution in this area. The method of heating or cooling of the cylinder to control the wake is not yet used.

Use of an acoustic source in the flow field is another method for controlling the vortex shedding. R. D. Blevins(1985) has showed the effect of sound on vortex shedding from cylinders. Frequency of vortex shedding can be shifted by sound applied above or below the nominal shedding frequency. It is also observed that the change is mainly because of the velocity induced by the sound and not by the sound pressure. For incompressible flows this is not a promising alternative as the velocity perturbed by the sound source is very small.

1.3 Aim and Scope of Present Work

The present work aims at developing a flow solver which solves the complete Navier-Stokes and the energy equation, and using the solver to study the following in the case of flow past a circular cylinder placed in a parallel plate horizontal channel:

- the effect of free convection in a low Reynolds number flow (Re $\sim$ 200) on the flow and heat transfer parameters

- the effect of length and location of splitter plate on vortex shedding
- the effect of suction and blowing on vortex generation

1.4 Organisation of Thesis

The present chapter (Chapter-1) contains introduction to the problem considered, its importance, literature available on the problem and the aim of the present work. Chapter-2 deals with the mathematical formulation of the two dimensional laminar flow. The governing equations are derived in its integral form. The solution procedure which uses some features of FEM in the control volume formulation is discussed in this chapter. For flow past circular cylinder, the results for mixed convection heat transfer, control of vortex shedding using splitter plate, and the influence of suction/injection from the cylinder surface are discussed in Chapter-3. The concluding remarks are highlighted in Chapter-4.

Chapter 2

Governing Equations and Solution Procedure

2.1 Derivation of Governing Equations

Towards numerically simulating the heat transfer and fluid flow past a circular cylinder placed between two parallel plates, the first task is the mathematical modeling of the problem. Since the present study is concerned with low Reynolds number flow, the flow is assumed to be laminar and two dimensional. To determine the fluid flow and thermal properties, the continuity, momentum, and energy conservation principles are applied over the domain of interest.Considering a typical control volume for mass continuity, **cv1**, the integral form of the mass balance can be written as

$$\frac{\partial}{\partial t}\int\int_{cv1} \rho \, dA + \int_{cs1} \rho \, \underline{V} \cdot \hat{n} \, dl = 0 \tag{2.1}$$

where, dl is an elemental length on the boundary **cs1** of the control volume **cv1**, and $\hat{n}$ is the local outward normal vector. For incompressible flow, the first term of the equation (2.1) is identically zero, which simplifies the equation to

$$\int_{cs1} \underline{V} \cdot \hat{n} \, dl = \int_{cs1} (u \, n_x + v \, n_y) \, dl = 0 \tag{2.2}$$

where, n_x and n_y are the direction cosines of the outward normal $\hat{n}$ on the boundary **cs1**.

Now considering any typical momentum control volume **cv2**, (the reason for considering different control volume for mass continuity and momentum balance is that the solution procedure used to solve the equations uses different control volumes) the integral form of x and y momentum balance equations can be written as

$$\frac{\partial}{\partial t}\int\int_{cv2} u\ (\rho\, dA) + \int_{cs2} u\ (\rho \underline{V}\cdot\hat{n}\, dl) = F_x \tag{2.3}$$

$$\frac{\partial}{\partial t}\int\int_{cv2} v\ (\rho\, dA) + \int_{cs2} v\,(\rho \underline{V}\cdot\hat{n}\, dl) = F_y \tag{2.4}$$

where F_x and F_y are the components of the resultant forces acting on the control volume in x and y directions respectively. These can be evaluated as

$$\begin{aligned} F_x &= \hat{i}\cdot\int_{cs2}\underline{\sigma}\cdot\hat{n}\, dl + \hat{i}\cdot\int\int_{cv2}\rho\,\underline{g}\, dA \\ &= \hat{i}\cdot\int_{cs2}\left\{-p\,\underline{I} + \mu\left(\underline{\nabla}\ \underline{V} + \underline{\nabla}\ \underline{V}^T\right) - \frac{2}{3}\mu\,(\nabla\cdot V)\,\underline{I}\right\}\cdot\hat{n}\, dl + \\ &\qquad \int\int_{cv2}\rho\, g_x\, dA \end{aligned}$$

where $\underline{\sigma}$ is the stress and g is the acceleration due to gravity. For incompressible flow

$$F_x = \int_{cs2}\left\{-p\,n_x + 2\mu\frac{\partial u}{\partial x}n_x + \mu\left(\frac{\partial u}{\partial y} + \frac{\partial v}{\partial x}\right)n_y\right\} dl + \int\int_{cv2}\rho g_x dA \tag{2.5}$$

For the y momentum equation,

$$F_y = \hat{j}\cdot\int_{cs2}\underline{\sigma}\cdot\hat{n}dl + \hat{j}\cdot\int\int_{cv2}\rho\underline{g}dA + \hat{j}\cdot\int\int_{cv2} g\,\rho\beta\,(T - T_\infty)dA$$

where T is the temperature, and the third term in the above equation is due to buoyancy force. For incompressible flow

$$\begin{aligned} F_y = &\int_{cs2}\left\{-p\,n_y + 2\mu\frac{\partial v}{\partial y}n_y + \mu\left(\frac{\partial u}{\partial y} + \frac{\partial v}{\partial x}\right)n_x\right\} dl + \\ &\int\int_{cv2}\rho g_y dA + \int\int_{cv2}\rho g\beta(T - T_\infty)dA \end{aligned} \tag{2.6}$$

For incompressible flow, the contribution due to gravity can be absorbed into the pressure term. With this simplification the final form of the x and y momentum equations can be written as

$$\rho\left\{\frac{\partial}{\partial t}\int\int_{cv2} u\,dA \;+\; \int_{cs2} u\;(u\,n_x \;+\; v\,n_y)\,dl\right\} = \int_{cs2}\left\{-p\,n_x + 2\mu\frac{\partial u}{\partial x}n_x + \mu\left(\frac{\partial u}{\partial y}+\frac{\partial v}{\partial x}\right)n_y\right\}dl \tag{2.7}$$

$$\rho\left\{\frac{\partial}{\partial t}\int\int_{cv2} v dA \;+\; \int_{cs2} v\;(u\,n_x \;+\; v\,n_y)\,dl\right\} = \int_{cs2}\left\{-p\,n_y \;+\; 2\mu\frac{\partial v}{\partial y}n_y + \mu\left(\frac{\partial u}{\partial y}+\frac{\partial v}{\partial x}\right)n_x\right\}dl + \int\int_{cv2}\rho\,g\,\beta\,(T-T_\infty)dA \tag{2.8}$$

Now considering a typical control volume, **cv2**, the integral form of energy equation can be written as

$$\frac{\partial}{\partial t}\int\int_{cv2} h(\rho dA) \;+\; \int_{cs2}(\underline{V}\,h)\cdot\hat{n}\,dl \;= \int_{cs2} k\nabla T\;\cdot n\,dl + \int\int_{cv2} S_h\,dA \tag{2.9}$$

where h is the specific enthalpy, k is the thermal conductivity, T is the temperature of the fluid, and S_h is the volumetric rate of heat generation. For the case with no heat source, S_h is identically equal to zero. For liquids

$$c\;\;\text{grad}\,T \;=\; \text{grad}\,h$$

where c is the specific heat at constant pressure. If c is constant, (which is a reasonable assumption for liquids)

$$h \;=\; cT$$

With this substitution, the energy equation becomes

$$\rho\left\{\int\int_{cv2} T dA + \int_{cs2} T\,(u\,n_x + v\,n_y)\,dl\right\} = \int_{cs2} \frac{k}{c}\left\{\frac{\partial T}{\partial x}n_x + \frac{\partial T}{\partial y}n_y\right\} dl \tag{2.10}$$

$$X = \frac{x}{D}\;;\; Y = \frac{y}{D}\;;\; U = \frac{u}{U_{ave}}\;;\; V = \frac{v}{U_{ave}}\;;\; \tau = \frac{tU_{ave}}{D};\; P = \frac{p}{\rho U_{ave}^2}\;;$$
$$\theta = \frac{T - T_\infty}{T_w - T_\infty}\;;\; Re = \frac{U_{ave}\,D}{\nu}\;;\; Gr = \frac{g\,\beta\,(T_w - T_\infty)\,D^3}{\nu^2}\;;\; Pr = \frac{\mu\,c_p}{k}$$

are the parameters used to nondimensionalize the equation of continuity (2.2), momentum (2.7,2.8) and the energy (2.10), and are expressed in the non-dimensional form as

$$\int_{cs1} (U\,n_x + V\,n_y)\,dl = 0 \tag{2.11}$$

$$\left\{\frac{\partial}{\partial\tau}\int\int_{cv2} U dA + \int_{cs2} U\,(Un_x + Vn_y)\,dl\right\} = \int_{cs2}\left\{-Pn_x + \frac{2}{Re}\frac{\partial U}{\partial X}n_x + \frac{1}{Re}\left(\frac{\partial U}{\partial Y} + \frac{\partial V}{\partial X}\right)n_y\right\} dl \tag{2.12}$$

$$\left\{\frac{\partial}{\partial\tau}\int\int_{cv2} V dA + \int_{cs2} V\,(Un_x + Vn_y)\,dl\right\} =$$
$$\int_{cs2}\left\{-Pn_y + \frac{2}{Re}\frac{\partial V}{\partial Y}n_y + +\frac{1}{Re}\left(\frac{\partial U}{\partial Y} + \frac{\partial V}{\partial X}\right)n_x\right\} dl + \frac{Gr}{Re^2}\int\int_{cv2}\theta dA \tag{2.13}$$

$$\left\{\frac{\partial}{\partial\tau}\int\int_{cv2}\theta dA + \int_{cs2}\theta\,(Un_x + Vn_y)\,dl\right\} = \int_{cs2}\left\{\frac{1}{PrRe}\left(\frac{\partial\theta}{\partial X}n_x + \frac{\partial\theta}{\partial Y}n_y\right) dl\right\} \tag{2.14}$$

2.2 Solution Procedure

2.2.1 Description of the Algorithm

The EXTRA-FLAG algorithm proposed by A.Mukhopadyay *et al*(1993) is extended to include the energy equation, and used to solve the equations (2.11) - (2.14). This algorithm is based on integral mass, momentum and energy balance applied over the non-orthogonal control volume. The integral flow equations are converted into algebraic form through numerical quadrature coupled with spatial interpolation of their nodal values In order to facilitate the numerical quadrature, each non-orthogonal quadrilateral control volume is mapped into a standard square cell with the help of local curvilinear coordinates. Explicit time marching is employed for the momentum equations using pressure field corresponding to the previous time level. The satisfaction of the continuity equation, on the other hand, is enforced in an implicit fashion by iteratively correcting the velocity and pressure fields. Basically the method of solution uses some features of FEM (interpolation and numerical quadrature) with the control volume approach applied in MAC, SIMPLE and related algorithms. A detailed illustration is given in the following text.

The domain of interest is discretized into small curvilinear quadrilateral cells, as shown in Figure 2.1. The velocity and temperature nodes are located at the vertices, and the pressure nodes are located at the centroids of each cell. This helps in avoiding pressure and velocity decoupling. The continuity control volumes (**cv1**) are formed by grid lines connecting velocity nodes (Figure 2.2) and the momentum control volumes (**cv2**) are formed by curvilinear quadrilaterals whose vertices are pressure nodes (Figure 2.3). Since the order of the momentum equations is one order higher than the continuity equation, the velocities have been interpolated using bi-quadratic functions, while applying the momentum principle. For the satisfaction of continuity, bilinear interpolation functions have been used to describe the velocity variables over the respective control volumes. It can be

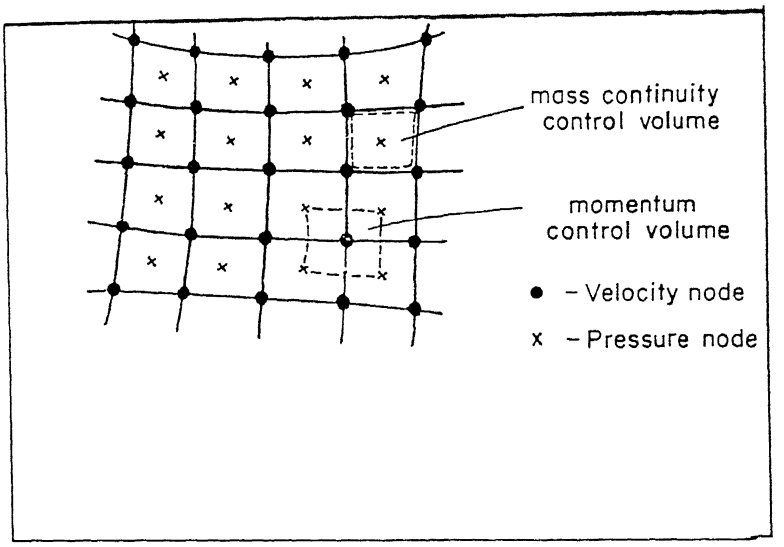

Figure 2.1: Schematic representation of the grid discretization

represented mathematically as follows. For the continuity equation

$$u = \sum_{k=1}^{4} M_k \, u_k \; ; \; v = \sum_{k=1}^{4} M_k \, v_k \tag{2.15}$$

and for the momentum equations

$$u = \sum_{k=1}^{9} N_k \, u_k \; ; \; v = \sum_{k=1}^{9} N_k \, v_k \tag{2.16}$$

The summation in equation (2.15) is performed by making use of velocities at the four vertices of the continuity control volume. Equation (2.16) uses the velocities of the neighbouring nodes of the corresponding momentum control volume. These are shown in Figure 2.4. The variation of the pressure over the momentum control volume is expressed in the form

$$p = \sum_{k=1}^{4} M_k \, p_k \tag{2.17}$$

In the equations (2.15) - (2.17), M_k, and N_k are the interpolation functions, and are given by

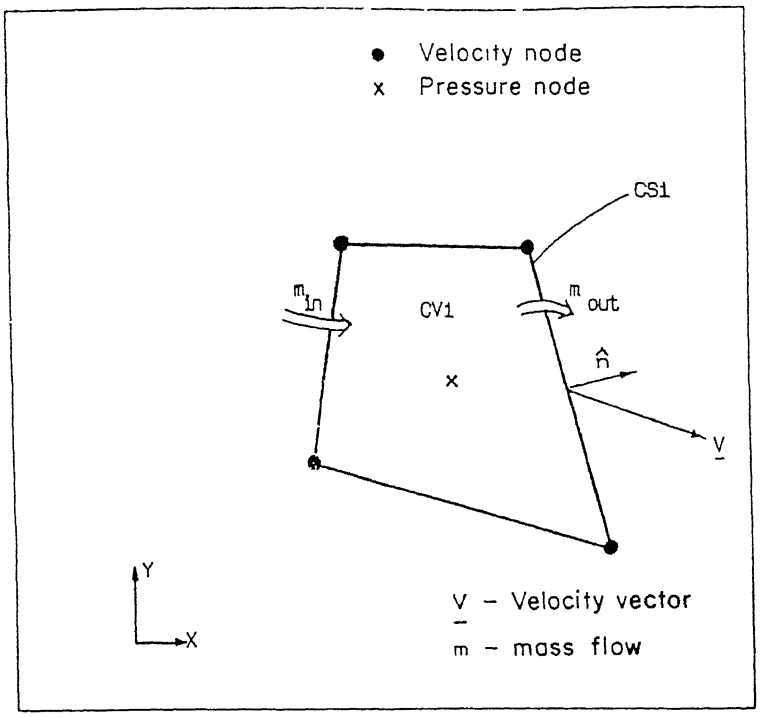

Figure 2.2: Mass balance over continuity cell (**cv1**)

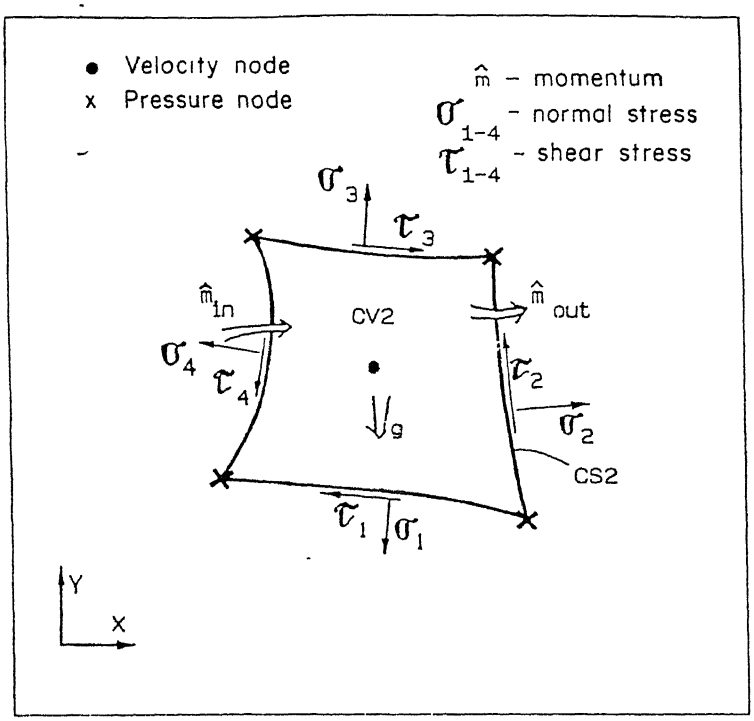

Figure 2.3: Momentum balance over momentum cell (**cv2**)

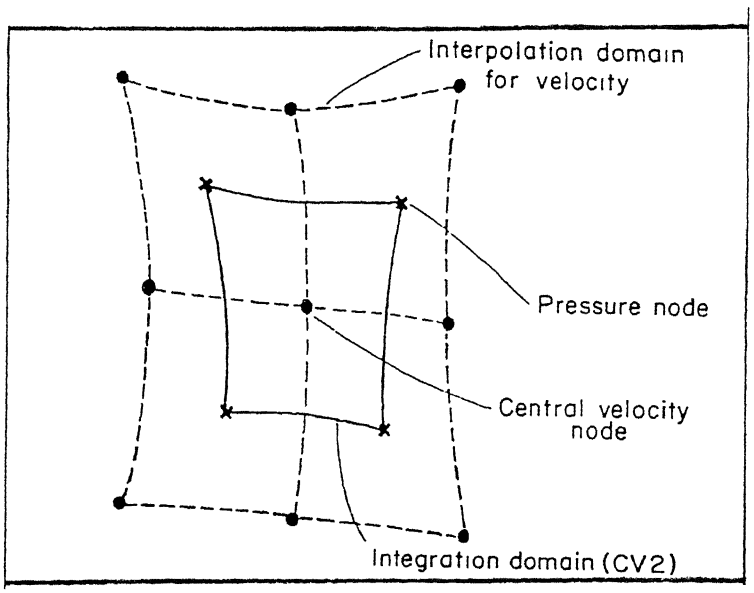

Figure 2.4: Interpolation domain for momentum balance

$$
\begin{aligned}
N_1 &= \frac{1}{64}\xi\eta\,(\eta-2)(\xi-2) \quad ; \quad N_2 = \frac{1}{32}\eta\,(4-\xi^2)(\eta-2) \\
N_3 &= \frac{1}{64}\xi\eta\,(\eta-2)(\xi+2) \quad ; \quad N_4 = \frac{1}{32}\xi\,(\xi+2)(4-\eta^2) \\
N_5 &= \frac{1}{64}\xi\eta\,(\eta+2)(\xi+2) \quad ; \quad N_6 = \frac{1}{32}\eta\,(4-\xi^2)(\eta+2) \\
N_7 &= \frac{1}{64}\xi\eta\,(\eta+2)(\xi-2) \quad ; \quad N_8 = \frac{1}{32}\xi(\xi-2)(4-\eta^2) \\
N_9 &= \frac{1}{16}(4-\xi^2)(4-\eta^2) \qquad \textit{and} \\
M_1 &= \frac{1}{4}(1-\xi)(1-\eta) \quad ; \quad M_2 = \frac{1}{4}(1+\xi)(1-\eta) \\
M_3 &= \frac{1}{4}(1+\xi)(1+\eta) \quad ; \quad M_4 = \frac{1}{4}(1-\xi)(1+\eta)
\end{aligned}
\tag{2.18}
$$

The integrals appearing in equations (2.11)-(2.14) have been evaluated using Gauss - Legendre quadrature. This is done by mapping the non-orthogonal control volume into a master cell whose co-ordinates vary from -1 to $+1$ in both the directions (Figure 2.5). The mapping is done through the isoparametric transformation. The coordinates x and y for any point within the non-orthogonal control volume are interpolated in terms of their nodal values in much the same way as the flow variables. The interpolation scheme for the

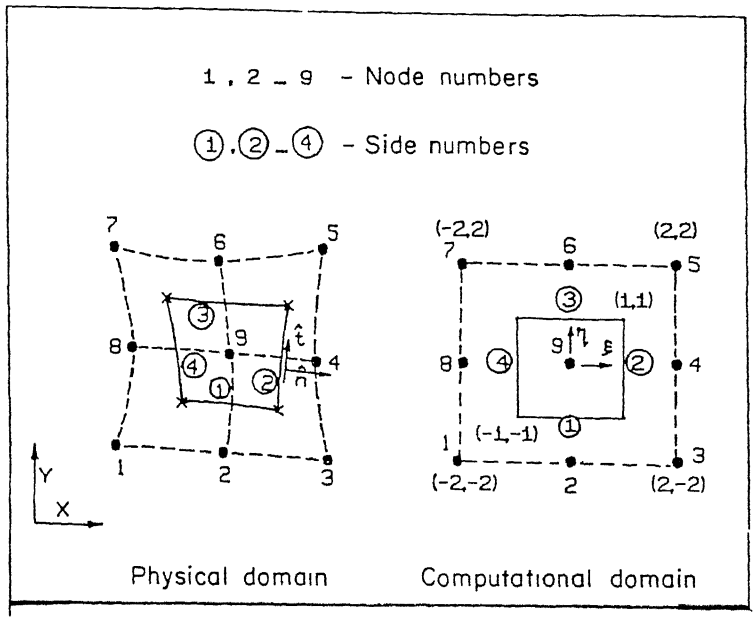

Figure 2.5: Transformation of a curvilinear control volume into a square computational cell

control volume **cv2** are given by

$$x = \sum_{k=1}^{9} N_k \, x_k \;\; ; \;\; y = \sum_{k=1}^{9} N_k \, y_k \tag{2.19}$$

where (x_k, y_k) are the coordinates of node surrounding the control volume as shown in Figure 2.4. For continuity cells (**cv1**), the linear transformation is used in the form

$$x = \sum_{k=1}^{4} M_k \, x_k \;\; ; \;\; y = \sum_{k=1}^{4} M_k \, y_k \tag{2.20}$$

With the above transformation the integrals appearing in the equations (2.11)-(2.14) can be rewritten in the form of transformed coordinates ξ and η. For all the mapped cells, ξ and η vary from -1 to $+1$, and because of it the Gauss-Legendre quadrature can be easily adopted for evaluating the integrals. The area integral is given by

$$\int_{-1}^{+1} \int_{-1}^{+1} F(\xi, \eta) \, d\xi \, d\eta \;\; = \;\; \sum_{k=1}^{m} \sum_{l=1}^{m} F(\xi_k, \eta_l) \, w_k \, w_l$$

where (ξ_k, η_l) are the Gauss points and w_k , w_l are the corresponding weights. The coordinates of the Gauss sampling points are the zeros of the m^{th} degree Legendre polynomials,

where m is the total number of Gauss points used in a particular direction. In the present case it is chosen to be equal to 2. The line integral can be evaluated as

$$\int_{-1}^{+1} F(\xi)\, d\xi = \sum_{k=1}^{m} F(\xi_k)\, w_k \quad \text{and}$$
$$\int_{-1}^{+1} F(\eta)\, d\eta = \sum_{k=1}^{m} F(\eta_k)\, w_k$$

For the completion of the transformation, it is necessary to convert the arc lengths, areas, surface integrals, derivatives and integrals in the physical coordinate system to the computational coordinates ξ and η. For the typical control volume (**cv2**), applying chain rule,

$$x = x(\xi, \eta) \quad ; \quad y = y(\xi, \eta)$$
$$dx = \frac{\partial x}{\partial \xi} d\xi + \frac{\partial x}{\partial \eta} d\eta \quad ; \quad dy = \frac{\partial y}{\partial \xi} d\xi + \frac{\partial y}{\partial \eta} d\eta$$

or in the matrix form

$$\begin{bmatrix} dx \\ dy \end{bmatrix} = \begin{bmatrix} \frac{\partial x}{\partial \xi} & \frac{\partial x}{\partial \eta} \\ \frac{\partial y}{\partial \xi} & \frac{\partial y}{\partial \eta} \end{bmatrix} \begin{bmatrix} \partial \xi \\ \partial \eta \end{bmatrix} = \begin{bmatrix} \sum_{k=1}^{9} \frac{\partial N_k}{\partial \xi} x_k & \sum_{k=1}^{9} \frac{\partial N_k}{\partial \eta} x_k \\ \sum_{k=1}^{9} \frac{\partial N_k}{\partial \xi} y_k & \sum_{k=1}^{9} \frac{\partial N_k}{\partial \eta} y_k \end{bmatrix} \begin{bmatrix} \partial \xi \\ \partial \eta \end{bmatrix}$$

in similar fashion, the derivatives can be obtained as

$$\begin{bmatrix} \frac{\partial}{\partial \xi} \\ \frac{\partial}{\partial \eta} \end{bmatrix} = \begin{bmatrix} \frac{\partial x}{\partial \xi} & \frac{\partial y}{\partial \xi} \\ \frac{\partial x}{\partial \eta} & \frac{\partial y}{\partial \eta} \end{bmatrix} \begin{bmatrix} \frac{\partial}{\partial x} \\ \frac{\partial}{\partial y} \end{bmatrix} = [J] \begin{bmatrix} \frac{\partial}{\partial x} \\ \frac{\partial}{\partial y} \end{bmatrix} \tag{2.21}$$

where $[J]$ is the Jacobian matrix for the transformation. The matrix in the above equation can be evaluated using equations (2.18) and (2.19) in the definition given above. From the equation (2.21), the velocity derivatives can be written as

$$\begin{bmatrix} \frac{\partial u}{\partial x} \\ \frac{\partial u}{\partial y} \end{bmatrix} = [J]^{-1} \begin{bmatrix} \frac{\partial u}{\partial \xi} \\ \frac{\partial u}{\partial \eta} \end{bmatrix} = [J]^{-1} \begin{bmatrix} \frac{\partial N_1}{\partial \xi} & \frac{\partial N_2}{\partial \xi} & \cdots & \frac{\partial N_9}{\partial \xi} \\ \frac{\partial N_1}{\partial \eta} & \frac{\partial N_2}{\partial \eta} & \cdots & \frac{\partial N_9}{\partial \eta} \end{bmatrix} \begin{bmatrix} u_1 \\ u_2 \\ . \\ . \\ . \\ u_9 \end{bmatrix} \tag{2.22}$$

Similarly we can write the equation for v and θ also.

On the sth side (s= 1,2,3,4) the elemental length vector dl_s can be written as

$$dl_s = dx_s\hat{\imath} + dy_s\hat{\jmath} = \left\{\left(\frac{\partial x}{\partial \xi}\right)_s d\xi + \left(\frac{\partial x}{\partial \eta}\right)_s d\eta\right\}\hat{\imath} + \left\{\left(\frac{\partial y}{\partial \xi}\right)_s d\xi + \left(\frac{\partial y}{\partial \eta}\right)_s d\eta\right\}\hat{\jmath} \quad (2.23)$$

The outward unit normal vectors on corresponding cell boundaries are given by

$$\hat{n}_s = \left\{\frac{\left(\frac{\partial y}{\partial \zeta}\right)_s \hat{\imath} - \left(\frac{\partial x}{\partial \zeta}\right)_s \hat{\jmath}}{\left(\frac{\partial l}{\partial \zeta}\right)_s}\right\} \cdot (-1)^m \quad (2.24)$$

where $m = 0$ for $s = 1,2$; $m = 1$ for $s = 3,4$ and

$$\left(\frac{dl}{d\zeta}\right)_s = \sqrt{\left\{\left(\frac{\partial x}{\partial \zeta}\right)_s^2 + \left(\frac{\partial y}{\partial \zeta}\right)_s^2\right\}}, \quad (2.25)$$

$\zeta = \xi$ for s =1,3 and $\zeta = \eta$ for s = 2,4. Also, the elemental length, dl is represented as

$$dl = \left(\frac{\partial l}{\partial \xi}\right)_s d\xi \quad (2.26)$$

for sides 1 and 3, since η is constant for these sides. Similarly

$$dl = \left(\frac{\partial l}{\partial \eta}\right)_s d\eta \quad (2.27)$$

for sides 2 and 4, since ξ is constant for these sides.

Lastly, the elemental area dA can be calculated by

$$dA = |J|\, d\xi d\eta \quad (2.28)$$

For continuity control volume, it is not necessary to employ the numerical quadrature, since the shape of **cv1** is simpler and the velocity interpolation is linear.

For the sake of simplicity, the final form of momentum and energy equations can be written in the matrix form

$$\begin{Bmatrix} \dot{u} \\ \dot{v} \\ \dot{\theta} \end{Bmatrix} = [[\mathbf{C}] + [\mathbf{D}]] \begin{Bmatrix} u \\ v \\ \theta \end{Bmatrix} + [\mathbf{S}]\{P\} + [\mathbf{Sr}] \quad (2.29)$$

where

$$[C] = \begin{bmatrix} C_{1_J} & 0 & 0 \\ 0 & C_{2_J} & 0 \\ 0 & 0 & C_{3_J} \end{bmatrix} \tag{2.30}$$

where

$$\begin{aligned} [C_{1_J}] = [C_{2_J}] = [C_{3_J}] &= \int_{cs2} N_J \left(u n_x + v n_y\right) dl \\ &= \sum_{s=1}^{4} \sum_{k=1}^{2} \left[N_J \sum_{q=1}^{9} \left(u_q n_x + v_q n_y\right) N_q \right] w_k \triangle l_p \end{aligned} \tag{2.31}$$

and

$$[D] = \begin{bmatrix} DU_{1_J} & DV_{1_J} & 0 \\ DU_{2_J} & DV_{2_J} & 0 \\ 0 & 0 & D\theta_{3_J} \end{bmatrix} \tag{2.32}$$

where

$$\begin{aligned} DU_{1_J} &= \frac{1}{\rho A_{cv2}} \int_{cs2} \left\{ 2\mu \frac{\partial N_J}{\partial x} n_x + \mu \frac{\partial N_J}{\partial y} n_y \right\} dl \\ &= \frac{1}{\rho A_{cv2}} \sum_{s=1}^{4} \sum_{k=1}^{2} \left[2\mu n_x \frac{\partial N_J}{\partial x} + \mu n_y \frac{\partial N_J}{\partial y} \right]_{k,s} w_k \triangle l_s \\ DU_{2_J} &= \frac{1}{\rho A_{cv2}} \int_{cs2} \left\{ \mu n_x \frac{\partial N_J}{\partial y} \right\} dl \\ &= \frac{1}{\rho A_{cv2}} \sum_{s=1}^{4} \sum_{k=1}^{2} \left[\mu n_x \frac{\partial N_J}{\partial y} \right]_{k,s} w_k \triangle l_s \\ DV_{1_J} &= \frac{1}{\rho A_{cv2}} \int_{cs2} \left\{ \mu n_y \frac{\partial N_J}{\partial x} \right\} dl \\ &= \frac{1}{\rho A_{cv2}} \sum_{s=1}^{4} \sum_{k=1}^{2} \left[\mu n_y \frac{\partial N_J}{\partial x} \right]_{k,s} w_k \triangle l_s \\ DV_{2_J} &= \frac{1}{\rho A_{cv2}} \int_{cs2} \left\{ \mu \frac{\partial N_J}{\partial x} n_x + 2\mu \frac{\partial N_J}{\partial y} n_y \right\} dl \\ &= \frac{1}{\rho A_{cv2}} \sum_{s=1}^{4} \sum_{k=1}^{2} \left[\mu n_x \frac{\partial N_J}{\partial x} + 2\mu n_y \frac{\partial N_J}{\partial y} \right]_{k,s} w_k \triangle l_s \\ D\theta_{3_J} &= \frac{1}{\rho A_{cv2}} \int_{cs2} \frac{k}{c} \left\{ \frac{\partial N_J}{\partial x} n_x + \frac{\partial N_J}{\partial y} n_y \right\} dl \\ &= \frac{1}{\rho A_{cv2}} \sum_{s=1}^{4} \sum_{k=1}^{2} \frac{k}{c} \left[\frac{\partial N_J}{\partial x} n_x + \frac{\partial N_J}{\partial y} n_y \right] dl \qquad \text{for } J = 1, 2, \ldots, 9 \,. \end{aligned} \tag{2.33}$$

The pressure matrix in turn is

$$[S] = \begin{bmatrix} S_{1_j} \\ S_{2_j} \\ 0 \end{bmatrix} \tag{2.34}$$

where

$$S_{1_j} = -\frac{1}{\rho A_{cv2}} \int M_j n_x dl = -\frac{1}{\rho A_{cv2}} \sum_{s=1}^{4} \sum_{k=1}^{2} (M_j n_x) w_k \triangle l_s$$

$$S_{2_j} = -\frac{1}{\rho A_{cv2}} \int M_j n_y dl = -\frac{1}{\rho A_{cv2}} \sum_{s=1}^{4} \sum_{k=1}^{2} (M_j n_y) w_k \triangle l_s$$

Lastly, the buoyancy term $[Sr]$ can be expressed as

$$[Sr] = \begin{bmatrix} 0 \\ Sr_2 \\ 0 \end{bmatrix}$$

with

$$Sr_2 = \frac{1}{\rho A_{cv2}} \int\int_{cv2} \rho g \beta (T - T_\infty) dA$$

$$= \frac{1}{\rho A_{cv2}} \sum_{l=1}^{2} \sum_{k=1}^{2} \rho g \beta (T - t_\infty) |J| w_k w_l$$

where θ_{ave} is the nondimensional temperature at the center of the control volume **cv2**.

The continuity equation can be discretized as

$$\sum_{s=1}^{4} (u_s n_{x,s} + v_s n_{y,s}) \triangle l_s = 0 \tag{2.35}$$

2.2.2 Upwinding of Convection Terms

In the numerical solution of Navier - Stokes equation, the convection terms need specific attention for conserving the transportive property. An effective upwind discretization for the convection terms is implemented by setting

$$CM_{1_j} u_j = CM_{2_j} u_j = \frac{1}{\rho A_{cv2}} \int (u n_x + v n_y) G_j u_j dl$$

where G_j is the upwind basis function, and is given by

$$\sum_{j=1}^{9} G_j u_j = \sum_{j=1}^{9} (1 - \alpha) N_j u_j + \alpha u_b$$

The subscript b corresponds to the node situated upstream of the concerned face and α is a fraction. For purely symmetric parabolic interpolation $\alpha = 0$ and for first order upwind interpolation, $\alpha = 1$.

2.2.3 Derivation of Pressure Correction Equation

When the time gradient of velocities and temperature are expressed in the discretized form, equation (2.29) becomes

$$\left\{ \begin{array}{c} u^{n+1} \\ v^{n+1} \end{array} \right\} = \left\{ \begin{array}{c} u^{n} \\ v^{n} \end{array} \right\} + \triangle t \left[\mathbf{CM}^n + \mathbf{DM}^n \right] \left\{ \begin{array}{c} u^{n} \\ v^{n} \end{array} \right\} + \triangle t \left[\mathbf{SM} \right] \left\{ p^{n+1} \right\} + \left[\mathbf{SR} \right] \left\{ \theta^n \right\} \quad (2.36)$$

where the subscripts n and $n+1$ denote time levels. However, at the start of calculation for each time step, p^{n+1} is not known and hence equation (2.36) predicts provisional velocities (represented by a superscript asterisk $*$) that satisfy momentum balance corresponding to the p^n pressures. When both pressure and velocities undergo iterative corrections, p^n takes up provisional value p^*. Thus

$$\left\{ \begin{array}{c} u^{*} \\ v^{*} \end{array} \right\} = \left\{ \begin{array}{c} u^{n} \\ v^{n} \end{array} \right\} + \triangle t \left[\mathbf{CM}^n + \mathbf{DM}^n \right] \left\{ \begin{array}{c} u^{n} \\ v^{n} \end{array} \right\} + \triangle t \left[\mathbf{SM} \right] \left\{ p^{*} \right\} + \left[\mathbf{SR} \right] \left\{ \theta^n \right\} \quad (2.37)$$

As the continuity equation is satisfied in each cell, all provisional velocities reach the final values for the present time step $(n+1)$. Subtracting equation (2.37) from equation (2.36) the expressions for the velocity corrections can be obtained as

$$\left\{ \begin{array}{c} u^{n+1} - u^{*} \\ v^{n+1} - v^{*} \end{array} \right\} = \left\{ \begin{array}{c} \delta u \\ \delta v \end{array} \right\} = \triangle t \left[\mathbf{SM} \right] \delta p \quad (2.38)$$

where δu, δv and δp are the velocity and pressure corrections, respectively. Applying the principle of continuity at the $(n+1)$ th level,

$$\sum_{s=1}^{4} (u_s^{n+1} n_{xs} + v_s^{n+1} n_{ys}) \triangle l_s = 0 \quad (2.39)$$

The unconverged velocities, however, do not satisfy the continuity equation, leading to a non-zero residue of the form

$$\sum_{s=1}^{4} (u_s^{*} n_{xs} + v_s^{*} n_{ys}) \triangle l_s = R \quad (2.40)$$

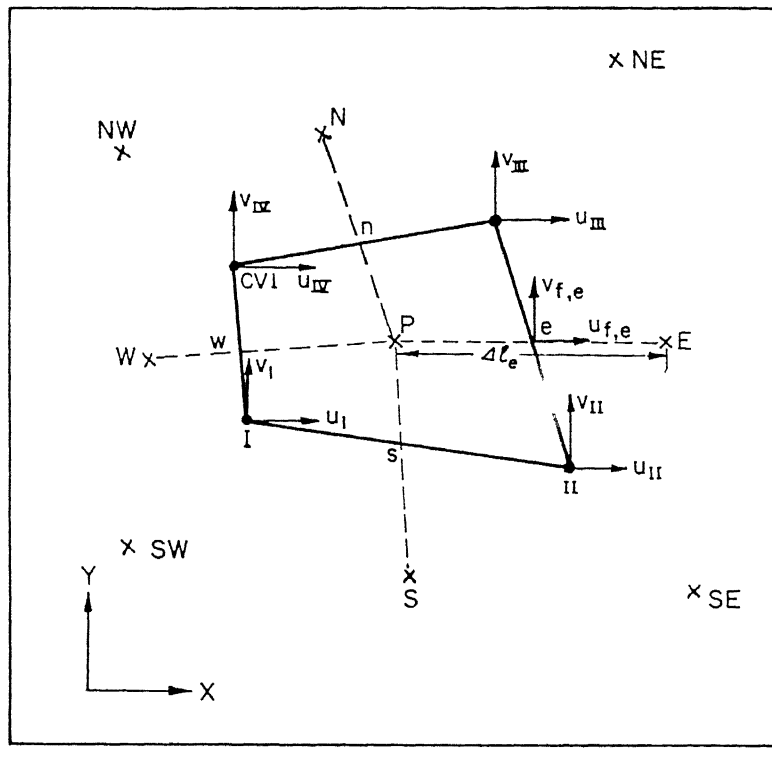

Figure 2.6: Pressure-velocity coupling for a continuity control volume

Subtracting equation (2.40) from equation (2.39), we obtain

$$\sum_{s=1}^{4}(\delta u_s\, n_{xs} \;+\; \delta v_s\, n_{ys})\triangle l_s = -R \tag{2.41}$$

where δu_s and δv_s are the average corrections on the sth side, so as to satisfy continuity principle in the control volume. The quantities δu_s and δv_s are expressed in terms of the nodal velocity corrections, which in turn are substituted by proper pressure correction terms using equation (2.38). These average velocity corrections, when evaluated as the simple average of the nodal velocities, lead to decoupling of pressure in alternate continuity cells which was also observed by Majumdar *et al*(1987).

Introducing face-center velocity corrections $\delta u_{f,s}, \delta v_{f,s}$ as shown in Figure (2.6), the average corrections on the east side of the **cv1** can be expressed as

$$\delta\overline{u}_e \;=\; \frac{1}{6}\delta u_{II} + \frac{1}{6}\delta u_{III} + \frac{4}{6}\delta u_{f,e}$$

$$\delta\overline{v}_e = \frac{1}{6}\delta v_{II} + \frac{1}{6}\delta v_{III} + \frac{4}{6}\delta v_{f,e} \tag{2.42}$$

where II and III are the velocity nodes lying on the east face. Similarly, the average corrections on other sides can also be estimated. Note that equation (2.42) amounts to the application of Simpson's rule along the boundaries of **cv1**. In order to find the expression for $\delta u_{f,e}$, $\delta v_{f,e}$ a modified form of the equation (2.38) can be written for the velocity correction vector as

$$\delta V = -\frac{\triangle t}{\rho}\nabla(\delta p) \tag{2.43}$$

eventually we can write

$$\begin{aligned} \delta u_{f,e} &= (\hat{i}\cdot\delta V)_{f,e} = -\frac{\triangle t}{\rho}\hat{i}\cdot\left\{\hat{e}\frac{\delta P_E - \delta P_P}{\triangle l_E}\right\} \\ \delta u_{f,e} &= \frac{\triangle t}{\rho}\left\{\frac{x_E - x_P}{\triangle l_E}\right\}\left\{\hat{e}\frac{\delta P_E - \delta P_P}{\triangle l_E}\right\} \end{aligned} \tag{2.44}$$

Similarly,

$$\delta v_{f,e} = \frac{\triangle t}{\rho}\left\{\frac{y_E - y_P}{\triangle l_E}\right\}\left\{\hat{e}\frac{\delta P_E - \delta P_p}{\triangle l_E}\right\} \tag{2.45}$$

Here $\hat{e}$ is the unit vector connecting the central pressure node P to the eastern neighbouring pressure node E. Similarly, the other face-center velocity corrections can be obtained as

$$\begin{aligned} \delta u_{f,(n,w,s)} &= \frac{\triangle t}{\rho}\frac{x_{(N,W,S)} - x_P}{\triangle l_{(N,W,S)}}\left\{\frac{\delta p_P - \delta p_{(N,W,S)}}{\triangle l_{(N,W,S)}}\right\} \\ \delta v_{f,(n,w,s)} &= \frac{\triangle t}{\rho}\frac{y_{(N,W,S)} - y_P}{\triangle l_{(N,W,S)}}\left\{\frac{\delta p_P - \delta p_{(N,W,S)}}{\triangle l_{(N,W,S)}}\right\} \end{aligned} \tag{2.46}$$

where the lower-case subscripts (n, w, s) refer to the corresponding boundary faces, while the upper-case subscripts (N, W, S) refer to the corresponding continuity cells. The mass residue contribution R_e to the east face is given by

$$\triangle l_e\left(\triangle u_e n_{xe} + \triangle v_e n_{ye}\right) = -R_e \tag{2.47}$$

Substituting for δu_e and δv_e from equation (2.42), we have

$$\triangle l_e \left\{ \frac{1}{6}\delta u_{II} + \frac{1}{6}\delta u_{III} + \frac{2}{3}\delta u_{f,e} \right\} n_{x,e} + \triangle l_e \left\{ \frac{1}{6}\delta v_{II} + \frac{1}{6}\delta v_{III} + \frac{2}{3}\delta v_{f,e} \right\} n_{y,e} = -R_e \quad (2.48)$$

From equation (2.38), the nodal velocity corrections are given by

$$\left\{ \begin{array}{c} \delta u_{II} \\ \delta v_{II} \end{array} \right\} = \triangle t \, [\mathbf{SM}]_{II} \{\delta p_S \;\; \delta p_{SE} \;\; \delta p_E \;\; \delta p_P\}^T \quad (2.49)$$

$$\left\{ \begin{array}{c} \delta u_{III} \\ \delta v_{III} \end{array} \right\} = \triangle t \, [\mathbf{SM}]_{III} \{\delta p_N \;\; \delta p_{NE} \;\; \delta p_E \;\; \delta p_P\}^T \quad (2.50)$$

It is to be noted that in equations (2.49), and (2.50), the pressure coefficient matrix SM is evaluated at nodes II and III. After substituting equations (2.44),(2.45),(2.49) and (2 50) into equation (2.48) , the residue contribution of the east face, R_e, can be calculated in terms of pressure corrections. Similar exercise for the other sides of the continuity cells would lead to a pressure correction equation of the form

$$[\mathbf{CP}] \{\delta P\} = -R \quad (2.51)$$

where CP is the coefficient matrix corresponding to the pressure correction array and R is the mass residue arising from velocities updated by momentum equations. For later iterations, the incremental residue is used in equation (2.51) which is calculated from equation (2.41). Equation (2.51) has a strong diagonal dominance ensuring smooth convergence with respect to iterations. Point-by-point iteration with successive over-relaxation has been employed to the pressure correction equations in the whole domain. The pressure and velocity corrections are iteratively improved until the corrections to the residues decrease below a predefined convergence level for all continuity cells (in the present case it is 1 $\times 10^5$).

2.3 Statement of the Problem

From the knowledge of flow past a circular cylinder, it can be said that the existence of a wake bubble behind the circular cylinder is observed for Re_D ¿. Beyond a Reynolds

number of 40, the wake loses its symmetry and vortex shedding starts. It is also observed that with partially confined walls the critical Reynolds number at which periodicity starts, grows with increasing blockage ration (which is defined by the ratio of diameter to the height of the channel). It is recognised from the above knowledge that the flow and heat transfer around a circular cylinder in a channel is characterized by

- the Reynolds number
- the blockage ratio (D/H)
- the velocity profile at the channel inlet, and
- the temperature difference between the fluid and surfaces.

A computational domain which consists of two solid walls with no-slip conditions and a circular cylinder placed between these walls (Figure 2.7), is selected for the present study. The blockage ratio of 0.25 is chosen for the study presented here Computation have been carried out with choosing the length of the channel L/H = 5. The geometric center of the cylinder is located at two diameters distance from the inlet.

For the implementation of numerical solution, the computational domain (Figure 2.7) is divided into a number of cells (Figure 2.8(a)). Figure 2.8(b) shows an enlarged portion of the mesh highlighting the zone surrounding the cylinder. A (251 $\times$ 51) grid is used for computation.

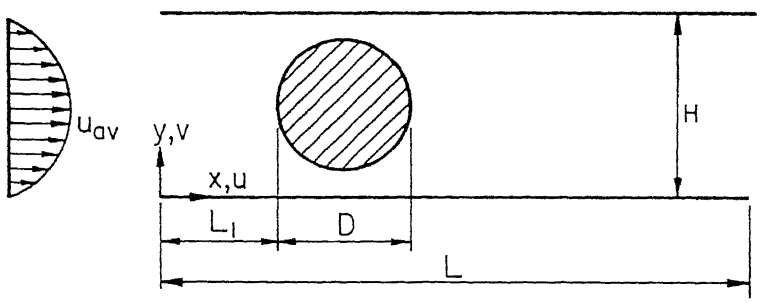

Figure 2 7: Schematic representation of the domain of study

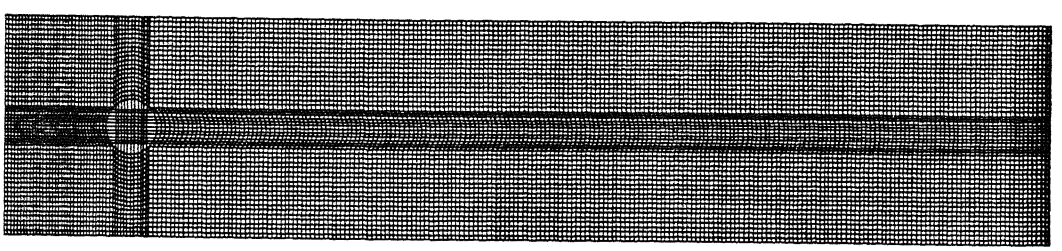

(a) full domain

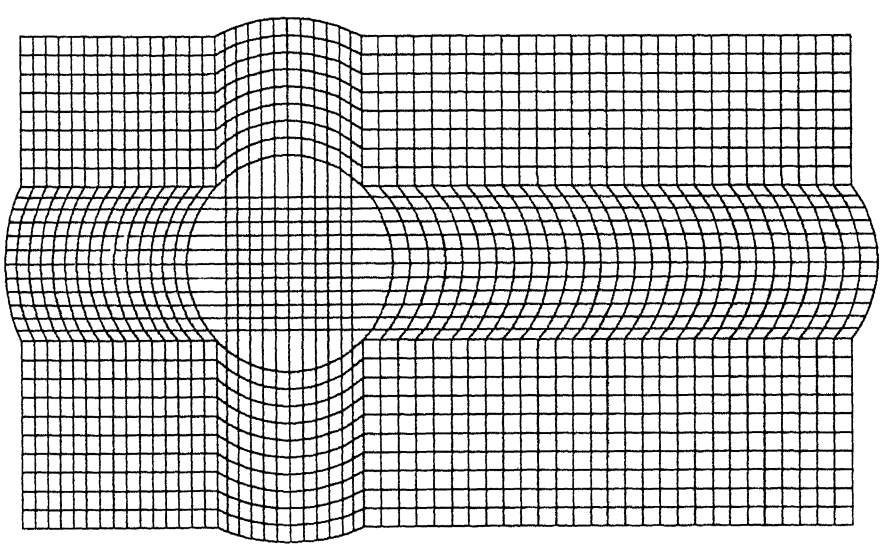

(b) grid around the cylinder

Figure 2.8: Mesh grid in the computational domain

2.4 Boundary Conditions

Fully developed velocity profile is assumed at the inlet. This will avoid the effect of growth of hydrodynamic boundary layer on the study parameters. It is assumed that the cylinder and walls are heated and maintained at some constant temperature. In this study it is assumed that both are at same temperature. No slip conditions are used on solid surfaces. At the exit, the derivative of independent variables are set to zero. Mathematically,

At the inlet

$$U = f(y^2) \; ; V = 0 \; ; \theta = 0$$

On Solid Surfaces

$$U = 0 \; ; \; V = 0 \; ; \theta = 1$$

At the outlet

$$\frac{\partial U}{\partial X} = 0 \; ; \; \frac{\partial V}{\partial X} = 0 \; ; \; \frac{\partial \theta}{\partial X} = 0$$

2.5 Closure

Equations governing the two dimensional laminar viscous fluid flow are derived in its integral form. A solution procedure which uses some features of FEM in the control volume formulation is presented and a computer code is developed to implement this algorithm. This code is used to study the the effect of thermal buoyancy on forced flow, control of vortex shedding using splitter plate, and influence of suction and blowing from the cylinder surface in the case of flow past circular cylinder. Results are presented in the next chapter.

Chapter 3

Results and Discussion

Effect of thermal buoyancy force, effect of the location and length of splitter plates, and the effect of suction and blowing from the cylinder surface on vortex shedding and related flow parameters, are studied numerically. Mixed convection (superimposition of thermal buoyancy force in the forced flow) may change the flow characteristics significantly when the flow Reynolds number is small and the temperature difference between the fluid and the solid surfaces is large. The effect of thermal buoyancy is discussed in the first section and is followed by discussion on the control of vortex shedding using splitter plate and suction and blowing.

3.1 Mixed Convection

The effect of thermal buoyancy on the skin friction and heat transfer rate is significant when the flow Reynolds number is low. Literature (G. Biswas ;1990) is available on this topic when the flow is steady. The present study is to investigate the influence of thermal buoyancy in an asymmetric flow regime. For this investigation, the Reynold number of the flow is chosen to be 200. Richardson number(Ri) is the ratio of thermal buoyancy force and the viscous force. Increase in Ri means that the magnitude of thermal buoyancy force is increasing, since the Reynolds number is kept constant The study is carried out for Ri= 0, 1, and 2. Skin friction coefficient, local Nusselt number variation, and the Strouhal

number ($St = \frac{Uf}{D}$ are the parameters considered to study the buoyancy effect.

Figure 3.1 shows the variation of the skin friction coefficient (C= $c_f Re$) on the channel walls. Skin friction coefficient is defined as

$$c_f = \mu \left.\frac{\partial u}{\partial y}\right|_{\text{wall}}$$

and in terms of the non-dimensional parameters

$$c_f = \frac{2}{Re} \left.\frac{\partial U}{\partial Y}\right|_{\text{wall}}$$

For forced convection flow, the skin friction coefficient increases as the flow approaches the cylinder and reaches its maximum at the center of cylinder. Because of vortex shedding, the skin friction coefficient on the channel walls in the downstream of the cylinder is oscillating. The magnitude of variation reduces as the flow moves downstream. This damping is mainly due to the confining walls. To study the the effect of thermal buoyancy, the skin friction coefficient is calculated for all the cases when the velocity signal measured at a point in the downstream reaches its peak. With mixed convection, the pattern of skin friction variation remains the same.

Figure 3.1(a) shows that when Ri is one, the maximum of skin friction (at the center of cylinder) increases. The point at which the skin friction coefficient is minimum is moved away from the cylinder when compared with the forced flow situation. The velocity profiles for these cases is given in Figure 3.2. Thermal buoyancy will result in inducing a velocity component in the upward direction. When the vortices are forming from the top half of the cylinder, the velocity resulting due to the thermal buoyancy is aiding the circulation of vortices. And when it is from the bottom half of the cylinder, thermal buoyancy opposes the circulation. This results in change in strength and size of vortices. This may be the cause of the shift in the minimum skin friction downstream. Further downstream, the skin friction with mixed convection behaves like forced convection flow. For Ri=2, the skin friction variation on the bottom wall is almost like pure forced convection flow. On the

top wall also the same trend of variation is seen (Figure 3.1(b)). But, for Ri=1, the skin friction coefficient decreases in contrast to the bottom wall. This is because the thermal buoyancy force causes the flow to move away from the surface at the bottom wall, and closer to the top wall. Here again, with $Ri = 2$, skin friction coefficient(C) is almost the same as that of forced flow situation. It may be mentioned that G. Biswas **et al** (1990) have observed that the maximum enhancement of heat transfer can be obtained through thermal buoyancy only when an optimum Gr and Re combination is used. Figure 3.3 shows the variation of local Nusselt number $\left(Nu_l = \frac{\partial T}{\partial y}\right)$ on the channel surfaces The steep gradient near the inlet shows the development of thermal boundary layer. Presence of cylinder in the flow field increases the local Nusselt number, which reaches its local maximum at the center of cylinder. This increase in Nu_l is due to the increase in flow velocity which results in higher convection. As the flow moves downstream, the Nusselt number approaches its value for thermally developed flow. The variation in the local Nusselt number is small with increase in Ri. At the bottom wall, increase in mixed convection results in increase in Nusselt number. Studying the variation of temperature in the flow field shows that the minima of the temperature profiles moves closer to the bottom wall. This leads to higher temperature gradient near the bottom wall and thus results in increased heat transfer. But at the top wall, increase in mixed convection results in reduced local Nusselt number. Because of unsteadiness in the main flow, the local Nusselt number also oscillates, and the size of oscillation reduces as the flow moves downstream.

Distribution of skin friction and local Nusselt number on the cylinder surface is given in Figure 3.4. Skin friction coefficient varies significantly in the wake region. Nusselt number increases in the wake region due to better mixing. This is because at this particular instant of time (normal component of velocity reaches its maximum at the point where the velocity is monitored), a vortex is forming near the top of the cylinder. As mentioned above the thermal buoyancy assists the flow and results in more convection. Variation in the local

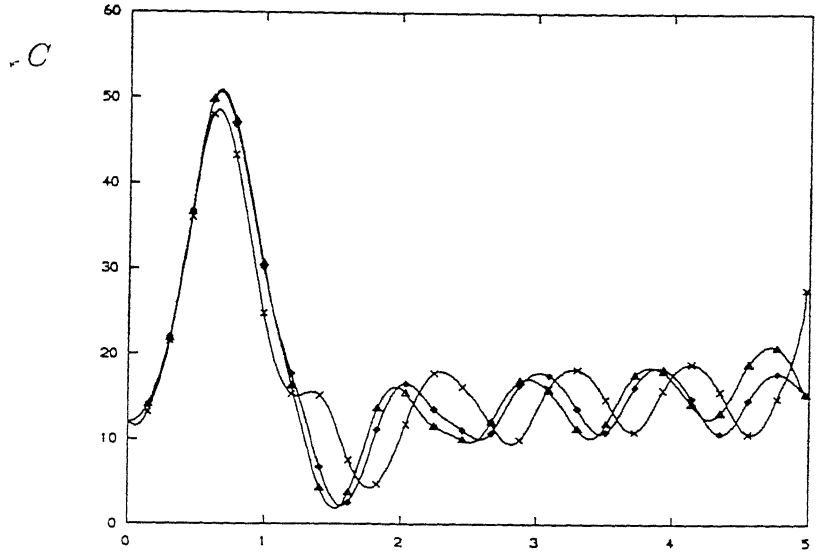

(a) Top wall

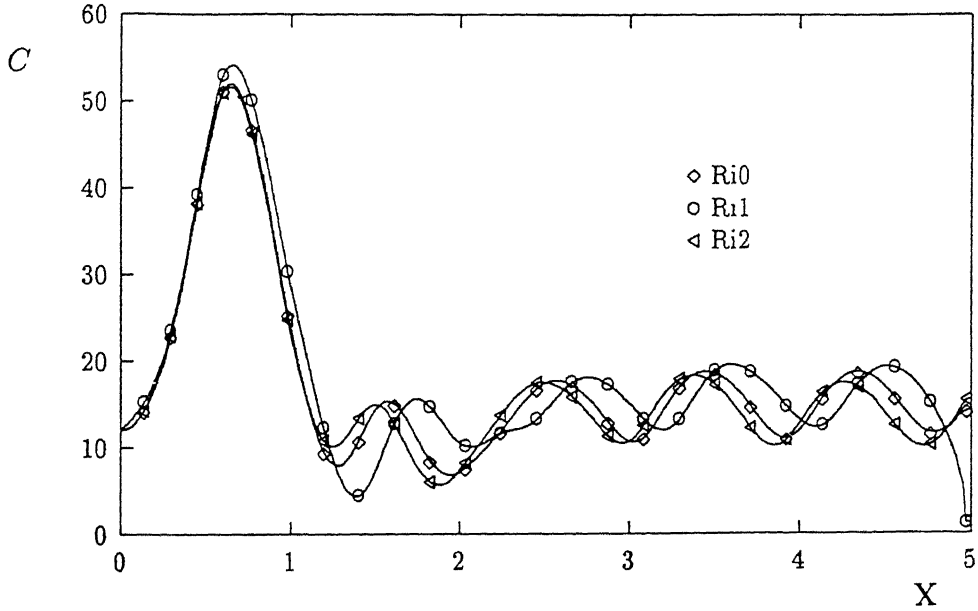

(b) Bottom wall

Figure 3.1: Skin friction variation on the channel walls

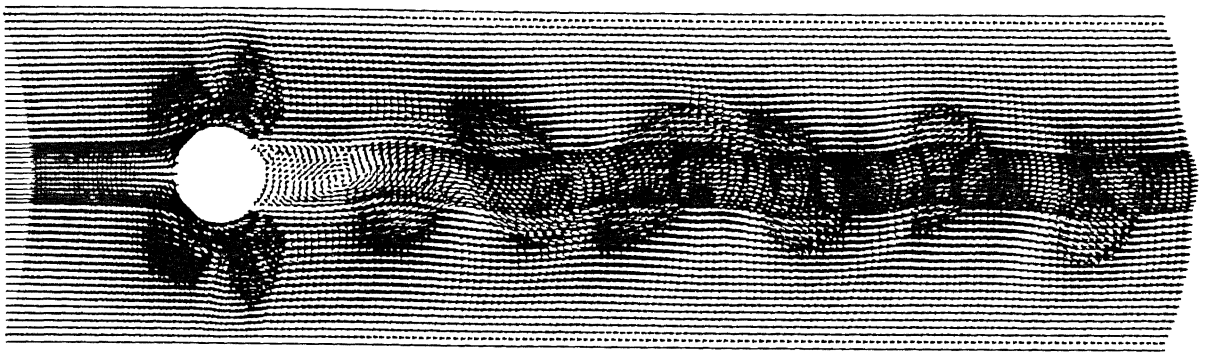

(a) Ri = 0

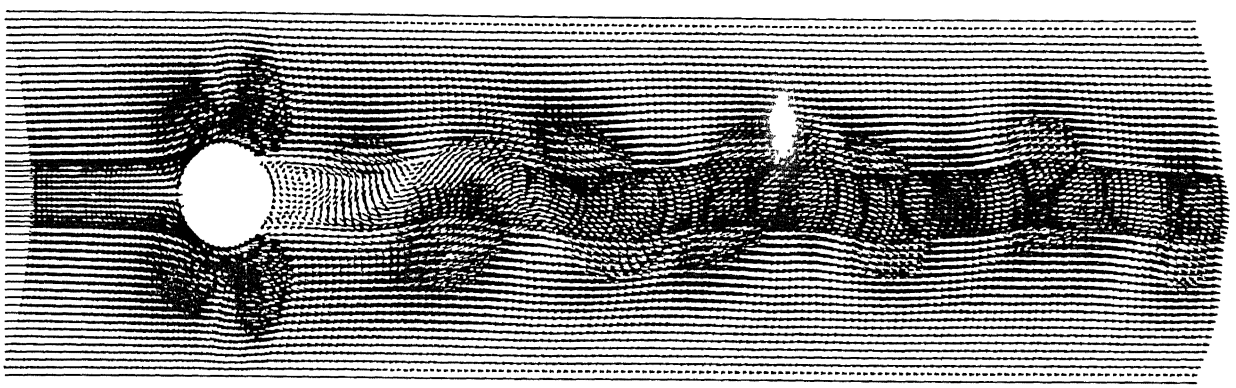

(b) Ri = 1

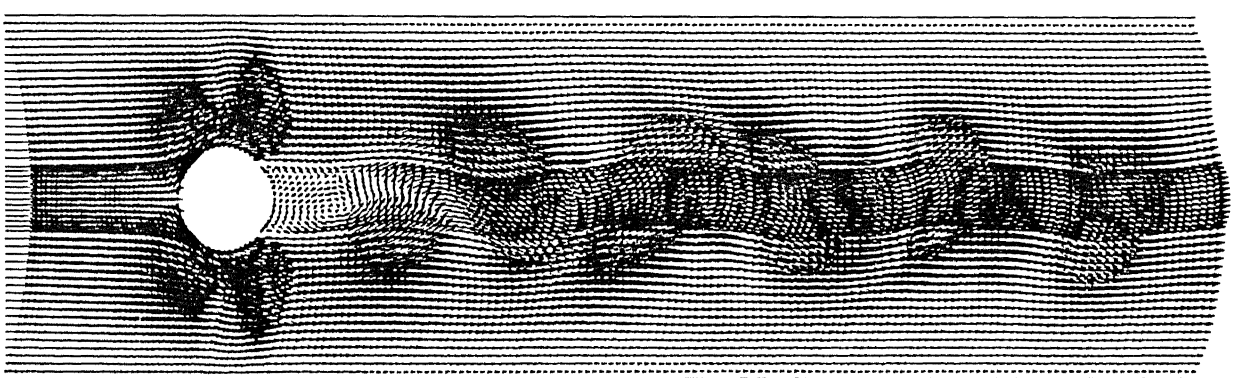

(c) Ri = 2

Figure 3.2: Velocity field for Ri=0,1, and 2

Nusselt number is very marginal on other points of the cylinder surface as the flow velocity at these points are high. Increase in the thermal buoyancy results in slight enhancement in heat transfer. Isothermal lines for all the cases are given in Figure 3.5, which helps in better understanding of distribution of temperature in the flow field. Uniform growth of thermal boundary layer is seen in the entrance region of the channel. Vortex shedding from the cylinder results in the wavy pattern of isothermal lines in the downstream. Using the velocity signal measured at a downstream location, the frequency of vortex shedding is calculated. Since there is no significant change in the signal, it is not shown here. The frequency spectrum of this signal(for Ri=0) is shown in Figure 3.6. Only one dominant frequency and very weak minor frequencies are seen. Variation in St with increase in Ri is very small (0.3450, 0.3467, and 0.3465 for Ri = 0,1, and 2 respectively). In the next section, the influence of splitter plate on vortex shedding is discussed.

3.2 Control of Vortex Shedding Using Splitter Plate

Use of a splitter plate in the downstream of the cylinder is one of the successful methods used for controlling vortex shedding. In the present study, the effect of length and location of splitter plate on vortex shedding are studied for Re=200. It is known from literature, that a splitter plate placed attached to the cylinder, and of length equal to five diameters, completely suppresses the vortex shedding for $Re < 5 \times 10^4$. In this study, the interest is to explore the possibilities of achieving the suppression with a shorter splitter plate. Four different configurations are studied. Placing the plate attached to the cylinder, two cases, that is, length equal to half the diameter, and length equal to the diameter, are studied. Then, keeping the plate one diameter away from the cylinder, computations have been carried out for axially aligned, and eccentric cases.

Figure 3.7(a) corresponds to the velocity signal for the uncontrolled case (without splitter

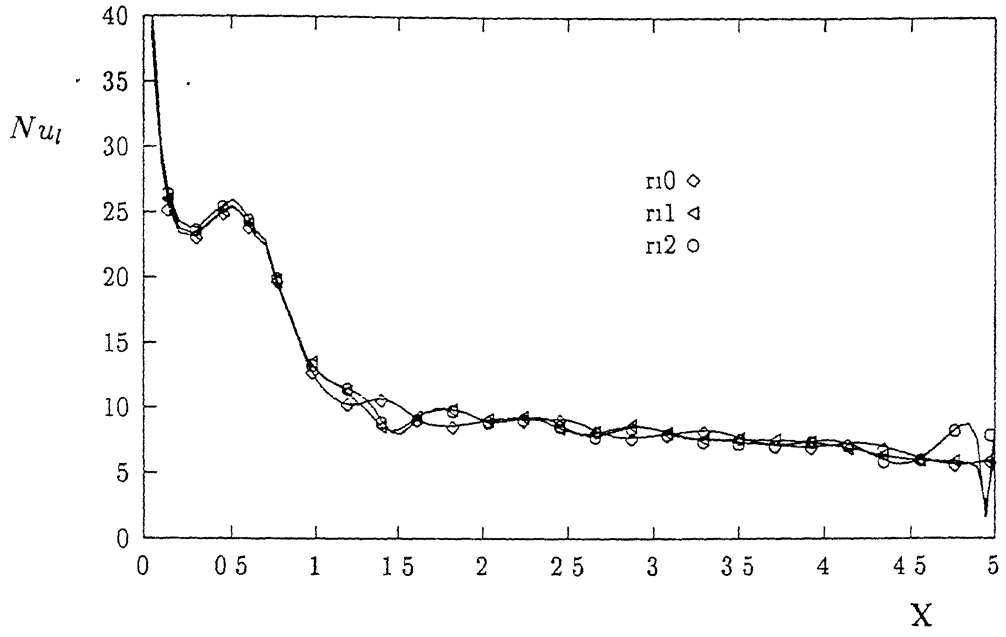

(a) Top wall

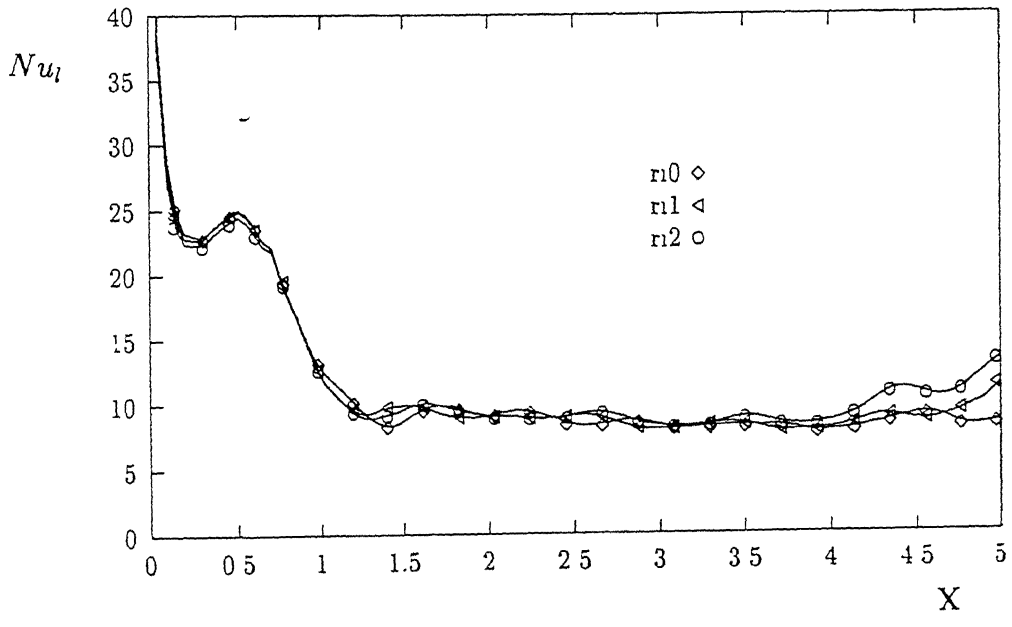

(b) Bottom wall

Figure 3.3: Variation of local Nusselt number on the channel walls

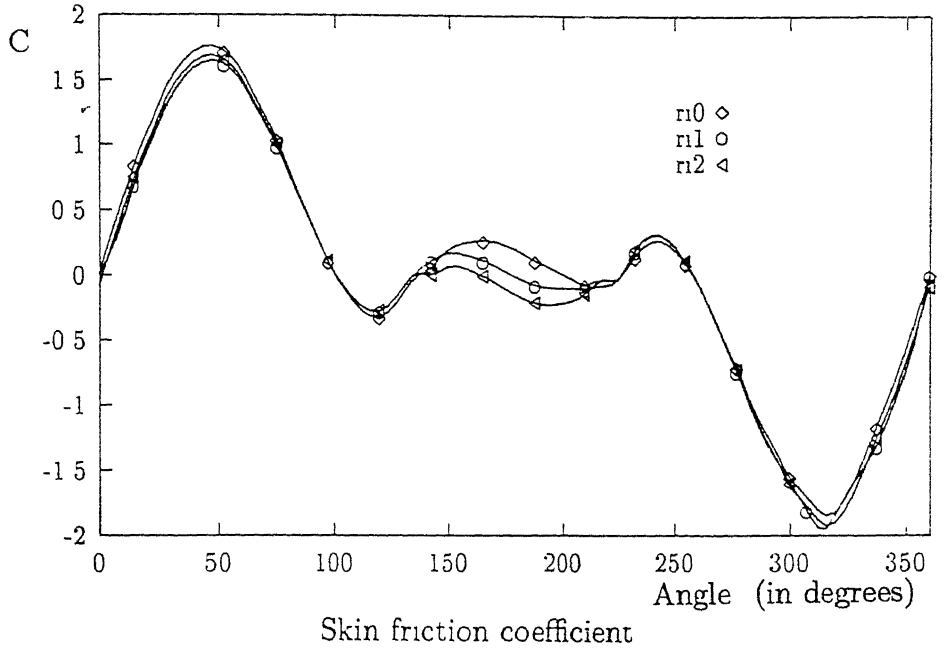

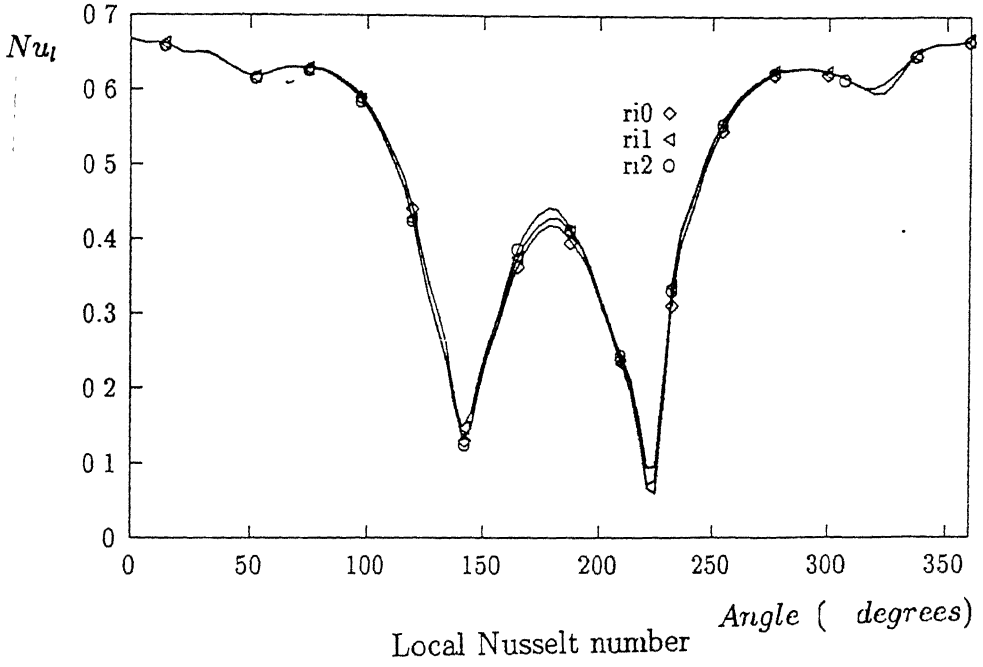

Figure 3.4: Skin friction and local Nusselt number distribution on the cylinder

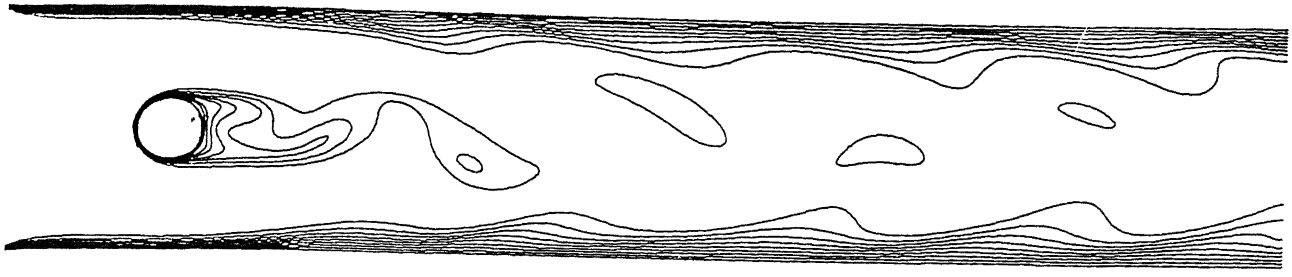

(a) Ri = 0

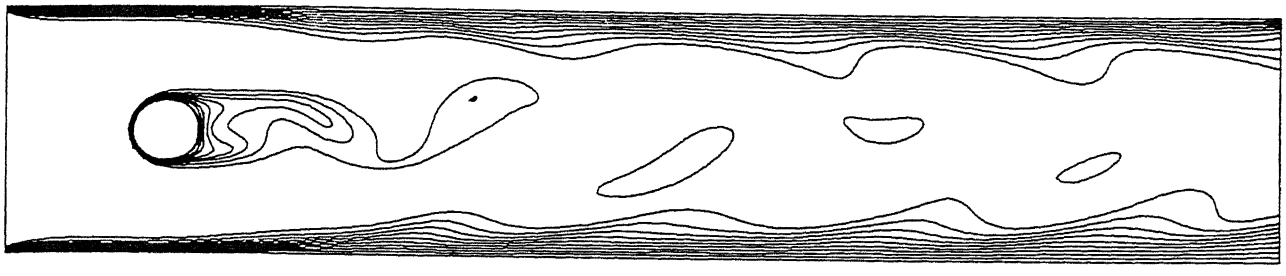

(b) Ri = 1

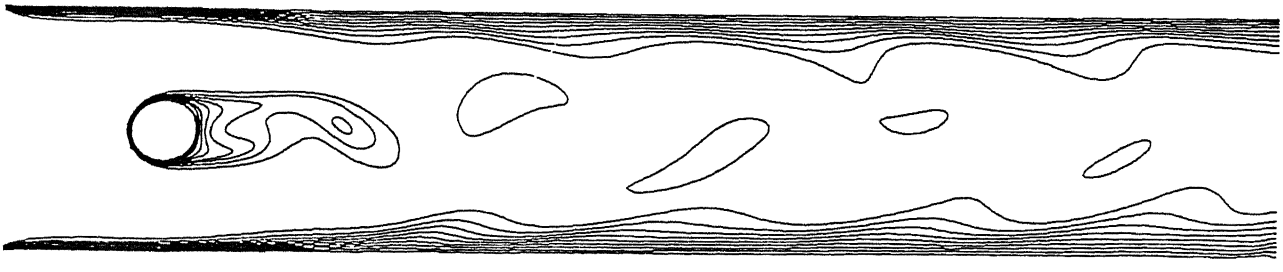

(c) Ri = 2

Figure 3.5: Isothermal lines in the flow field for Ri=0,1, and 2

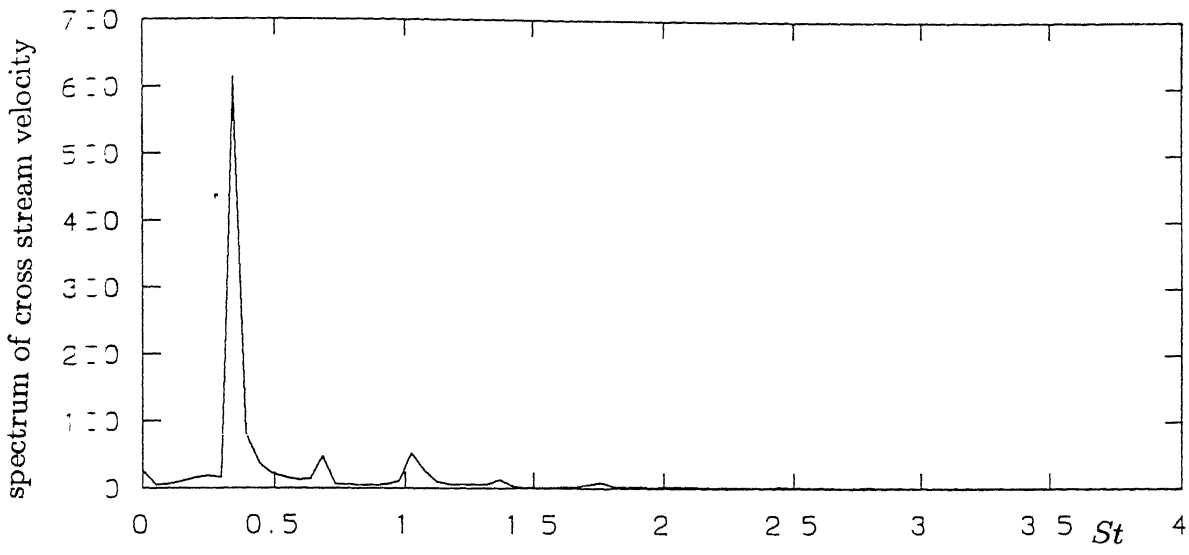

Figure 3.6: Spectrum of transverse velocity fluctuation in the near wake

plate). Figure 3.7(b) shows the normal velocity fluctuation when the splitter plate is placed attached to the cylinder. Normal velocity signal is monitored at the same location for all the cases (three diameters from the cylinder base). Comparing with the uncontrolled case, the magnitude of velocity fluctuation is reduced. From Figure 3.7(c), it can be seen that the formation of vortices is shifted downstream by a distance equal to the length of the plate. This results in increase in base pressure on the cylinder which reduces the drag force. Taking a FFT of the velocity signal, it is found that (it may be mentioned that fully developed velocity profiles is used at the inlet in all these studies) there is slight reduction in the St from 0.3450 to 0.3353. It is also observed that the flow is symmetric up to the end of splitter plate. Vortex generation is shifted downstream, resulting in more uniform streamlines (Figure 3.7(d)) Figure 3.7(e) shows the isothermal lines in the flow field. It is clear from this Figure, that because of vortex generation, the isothermal lines are not symmetric.

When the length of the splitter plate is increased from half diameter to one diameter, fluctuation in the normal velocity (Figure 3.8(a)) is still reduced. From this one may infer that the flow is approaching the steady state. But the St increases significantly and has

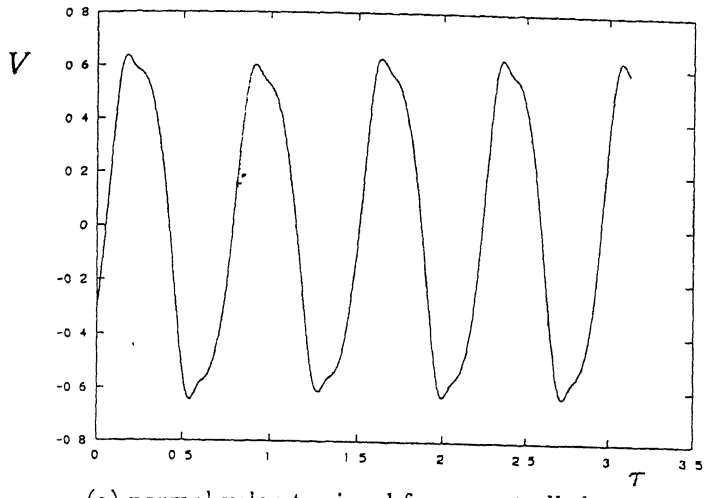

(a) normal velocity signal for uncontrolled case

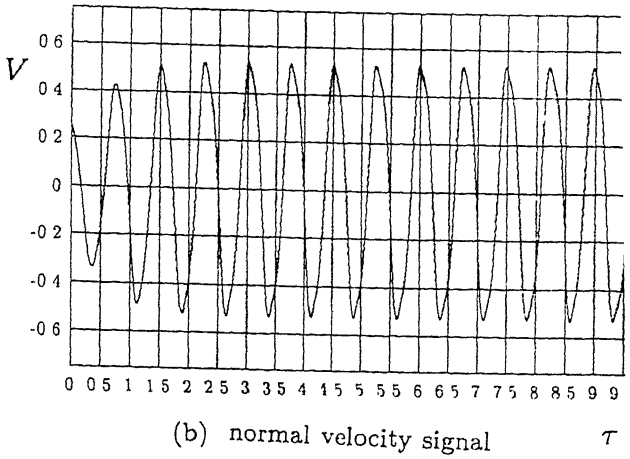

(b) normal velocity signal

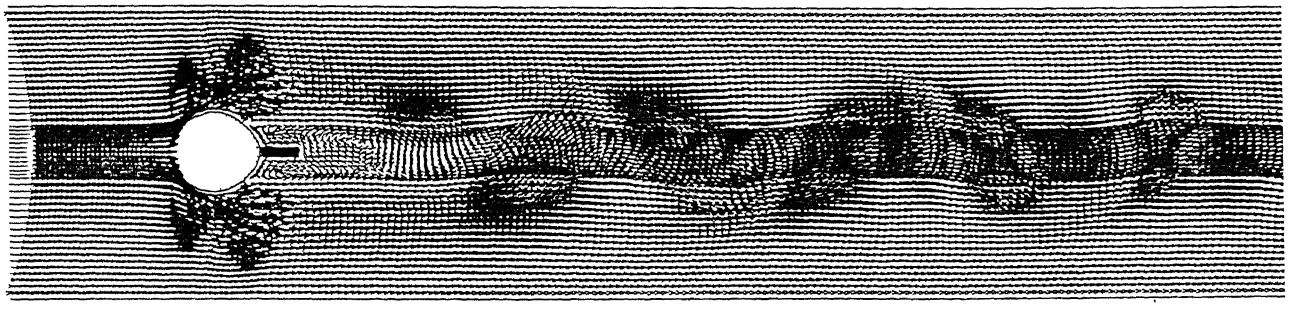

(c) Velocity profile

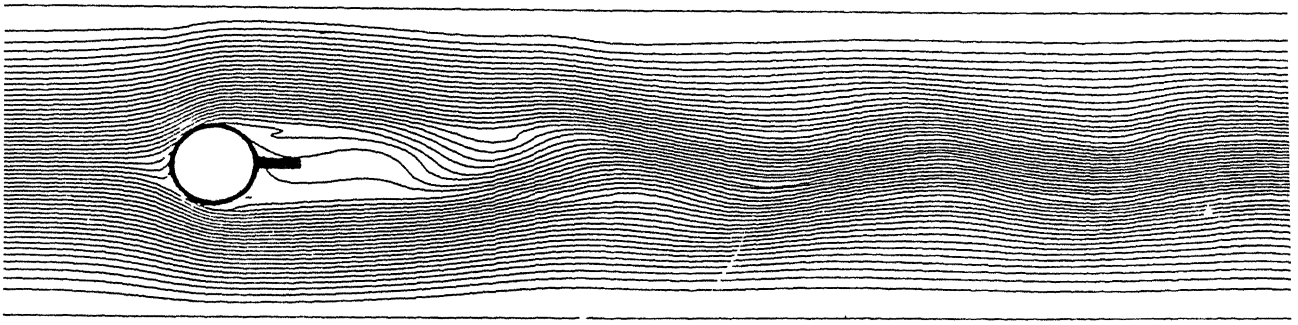

(d) Streamlines

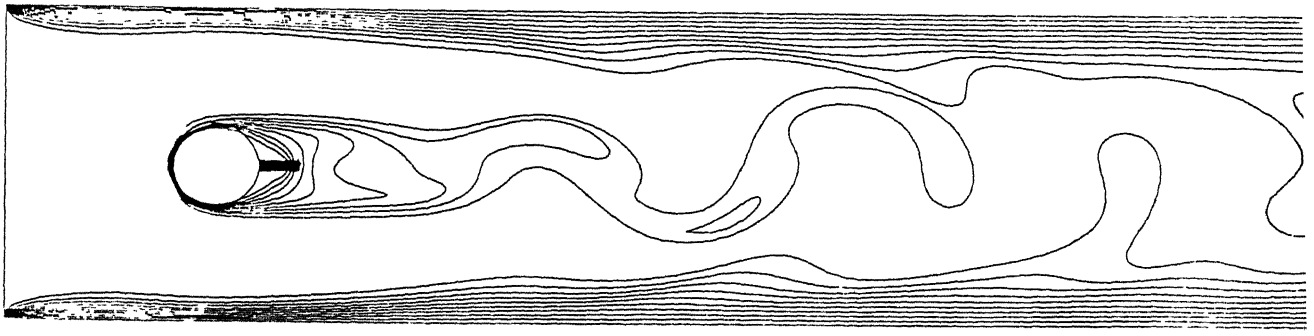

(e) Isotherm

Figure 3.7: Splitter plate attached, length = 1/2 diameter

a value 0.3472. The vortices generated from the cylinder interact with each other and the time of interaction dictates the vortex shedding frequency. It is seen that placement of splitter plate in the flow field produces tip vortices at the end of the plate. The size and strength of the vortices will vary with the length of the plate. The secondary vortices generated at the tips can be either same or opposite in nature (in rotational direction) with the main vortices. Secondary vortices of opposite nature actively interacts with the main vortices. This results in reduced interaction of main vortices and increased St. If the vortices are of same nature, secondary vortices do not interact with the main vortices and results in longer interaction time between the main vortices This reduces the value of St This is the reason for decrease and increase in St with different lengths of splitter plates. It is seen (Figures 3.8(b), 3.8(c)) that introduction of splitter plate makes the flow symmetric up to the end of the plate. This results in the reduced fluctuation of the velocity and more uniform streamlines. Isotherms (Figure 3.8(d)) are not disturbed near cylinder region, as they are more uniform just after the cylinder.

It is clear from the above studies that with attached splitter plate of length less than or equal to the diameter, suppression of vortex shedding is not possible, but a change in St can be achieved. Placing the plate attached to the cylinder reduces the fluctuation in the velocity in the wake, and shifts the formation of vortices further downstream. Instead of further increasing the length of splitter plate, placing the plate in the downstream is studied and the results are discussed below.

Figures 3.9(a) and 3.9(b) show the velocity profiles and streamlines when the plate of length equal to the diameter of the cylinder is shifted downstream by a distance equal to the diameter axially. Presence of a object in the downstream results in pressure disturbance, which will be convected to the upstream. This pressure disturbance affects the flow in the wake. When the plate is placed at some distance, the pressure disturbance will be

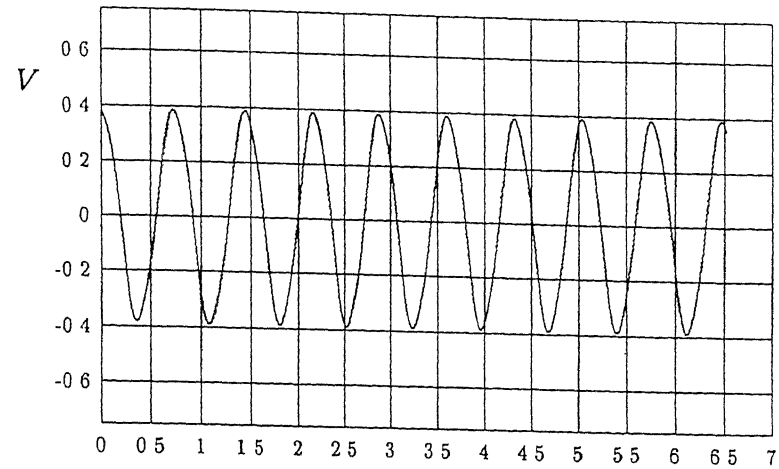

(a) normal velocity signal

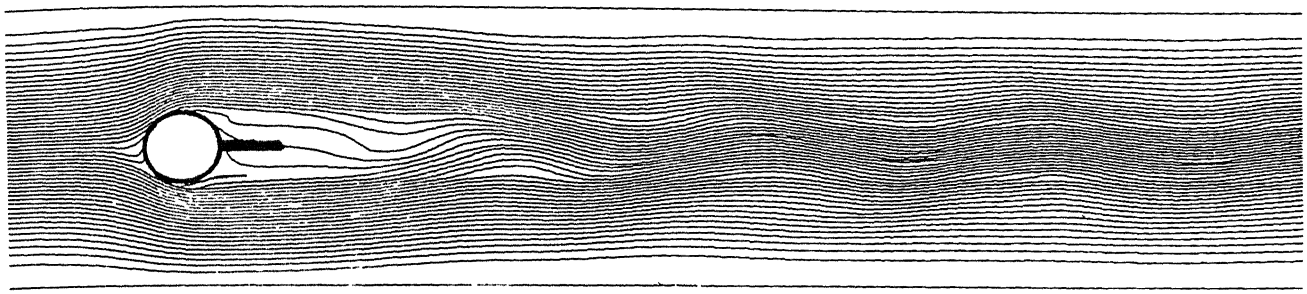

(b) Streamlines

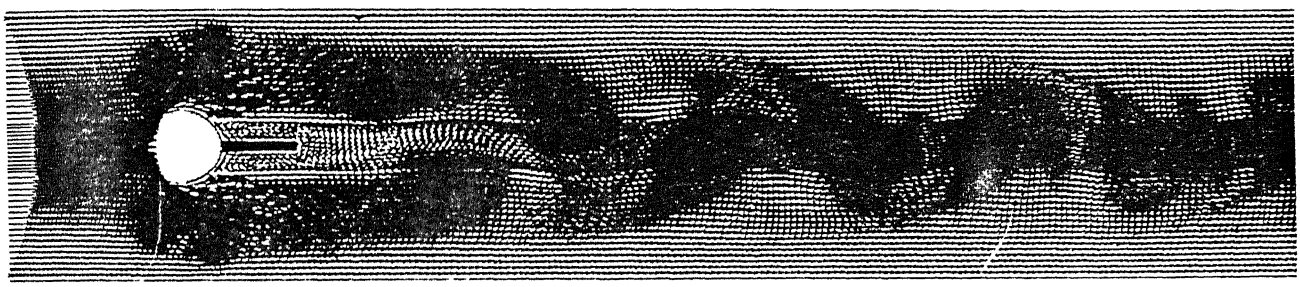

(c) Velocity profile

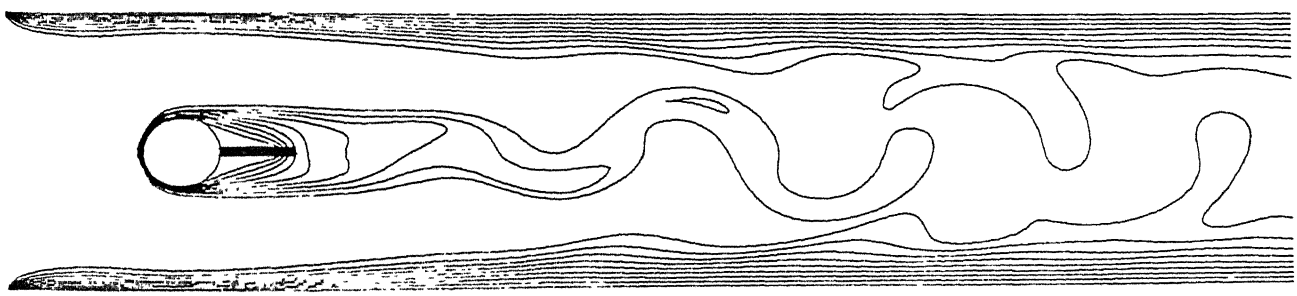

(d) Isotherm

Figure 3.8: Splitter plate attached, length = diameter

such that it increases the base pressure and reduces the drag force on the cylinder. Grinstein *et al* (1991) have observed that this length is approximately equal to one diameter for a square cylinder obstacle. When the plate is at the above said configuration, complete suppression of vortex shedding results. Two attached vortices are formed. Figure 3.9(c) shows the isothermal lines which are symmetric because of absence of vortex shedding.

The effect of placing the splitter plate of length equal to one diameter at an eccentric position is shown in Fig. 3.10. The plate is placed one diameter distance away from the cylinder and moved one fourth of the diameter moved upward from the central axis. Figure 3.10(a) shows that the shedding is very weak as the fluctuation in velocity is very small. Figure 3.10(b) shows the velocity profiles and it can be seen that there are formation of vortices which are of small size. Streamlines shown in Figure 3 10(c) supports this observation as the streamline at the center of flow field does not fluctuate much. Isothermal lines (Figure 3.10(d)) shows that the fluctuation in the flow field is very small as the temperature contours near the wall do not get disturbed much. Comparing with the bottom half of the flow, there is much disturbance in the upper half of flow field. It may be mentioned that the splitter plate is placed near the top wall. It is also observed that the temperature which is convected from the cylinder does not spread over the entire domain as the flow is not disturbed much.

Figure 3.11 shows the variation of skin friction on the top and bottom wall of the channel. Placing splitter plate in the wake attached to the cylinder increases the skin friction near the cylinder. The point of low skin friction is delayed with splitter plate. The fluctuation in the skin friction coefficient is due to the velocity fluctuation in the main flow. It can be seen that for both the walls, the fluctuation is zero with detached axially placed plate, because of steady flow. Eccentrically placed plate (detached) results in very small fluctuation as a result of weak shedding. Attached plates follows the trend of uncontrolled case

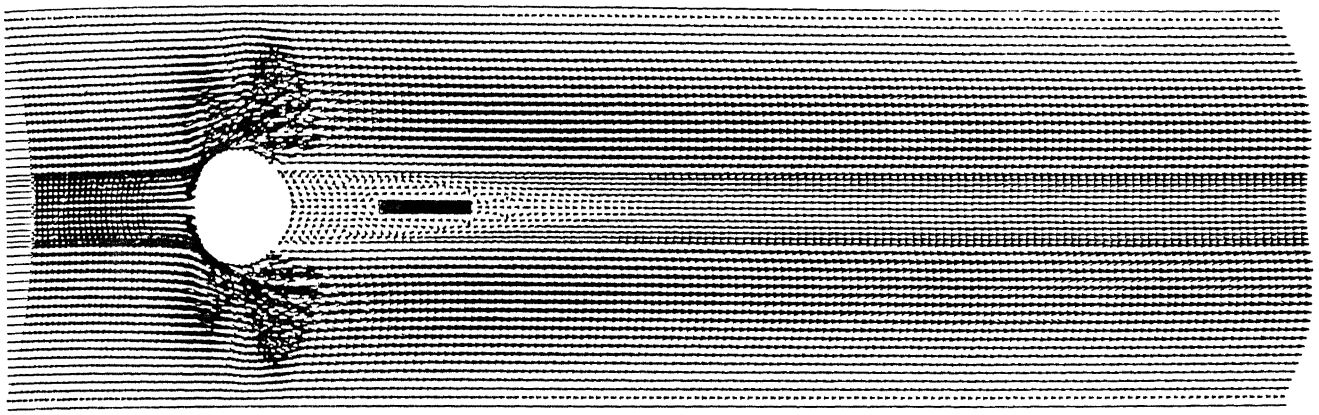

(a) Velocity profile

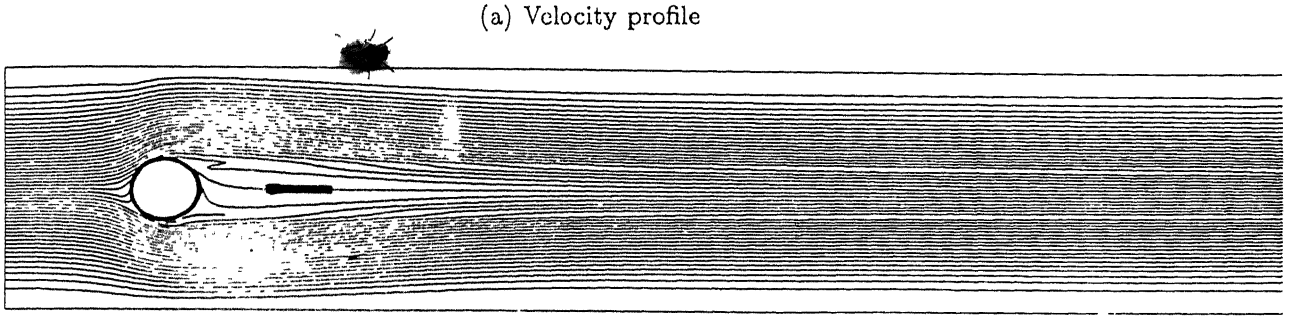

(b) Streamlines

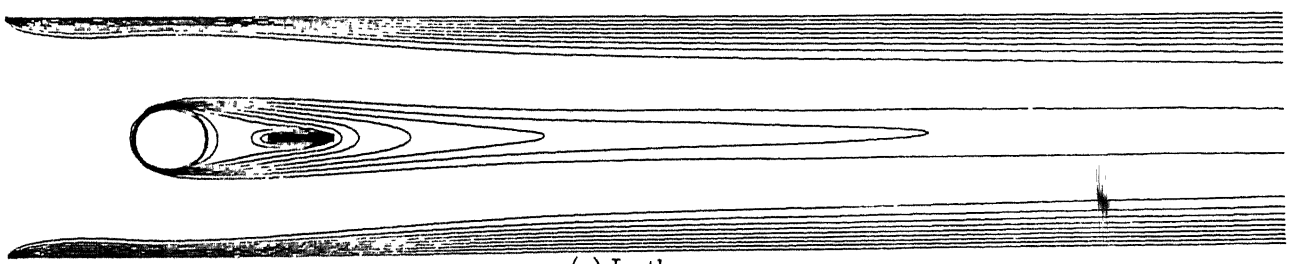

(c) Isotherm

Figure 3.9: Splitter plate detached from the cylinder, length = diameter

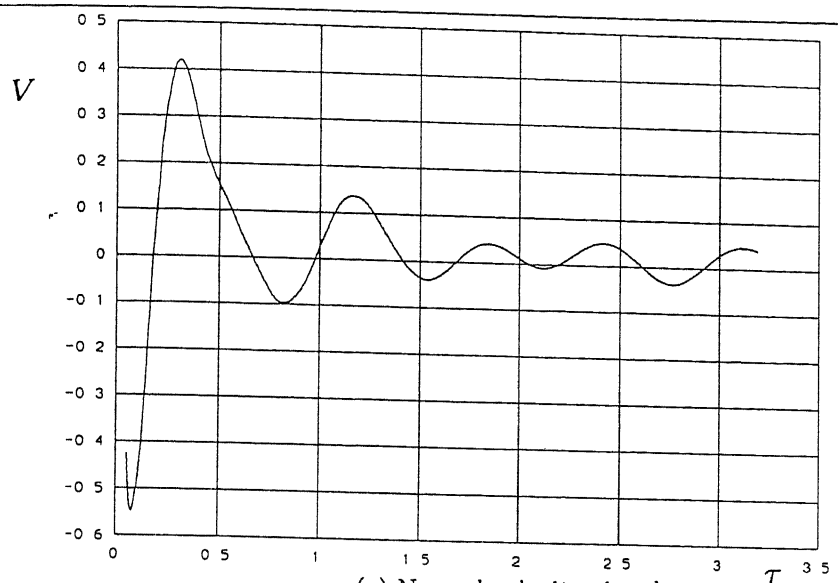

(a) Normal velocity signal

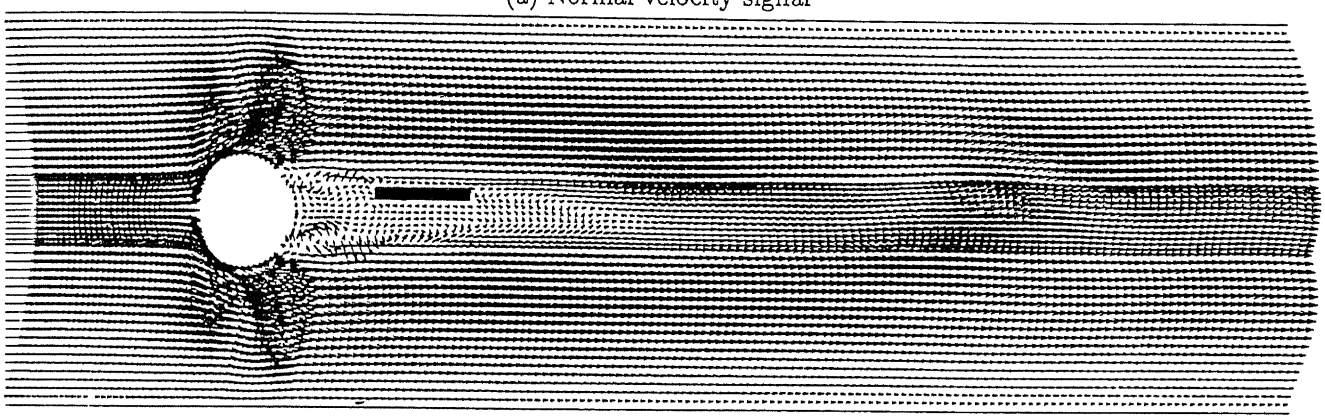

(b) Velocity profile

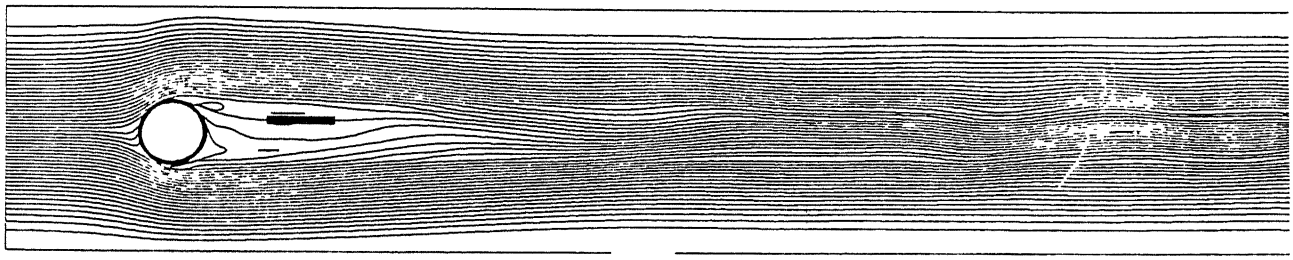

(c) Streamlines

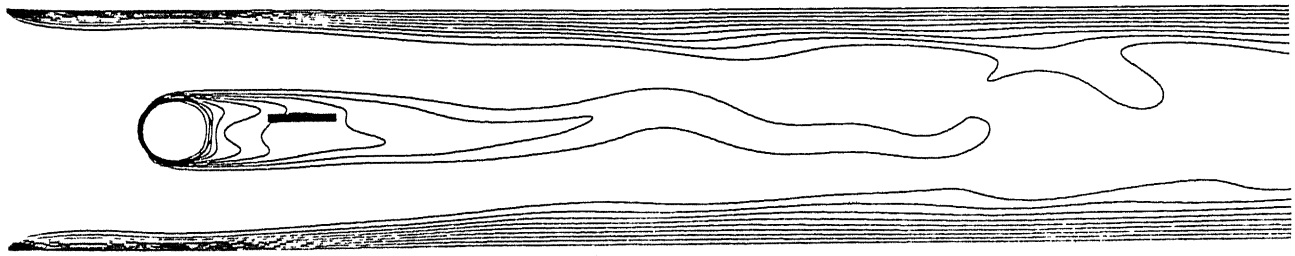

(d) Isotherm

Figure 3.10: Splitter plate detached from the cylinder, eccentric, length = diameter

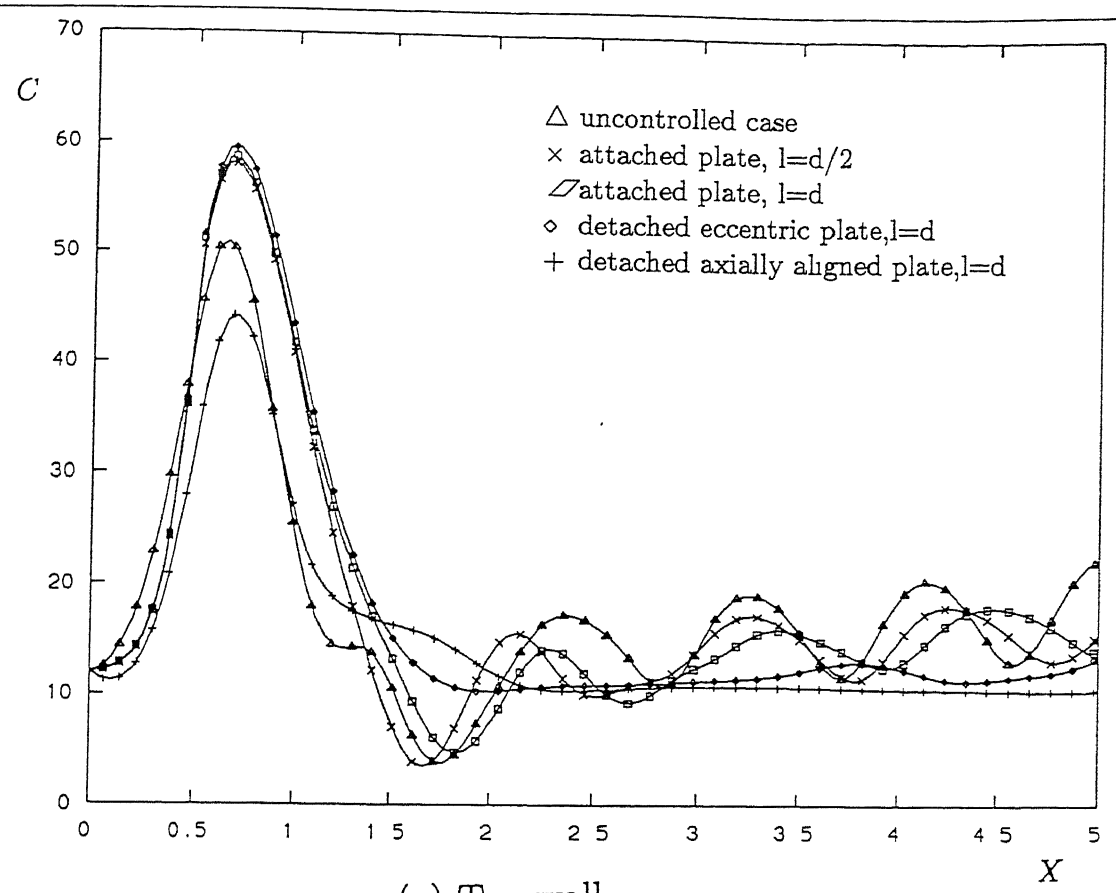

(a) Top wall

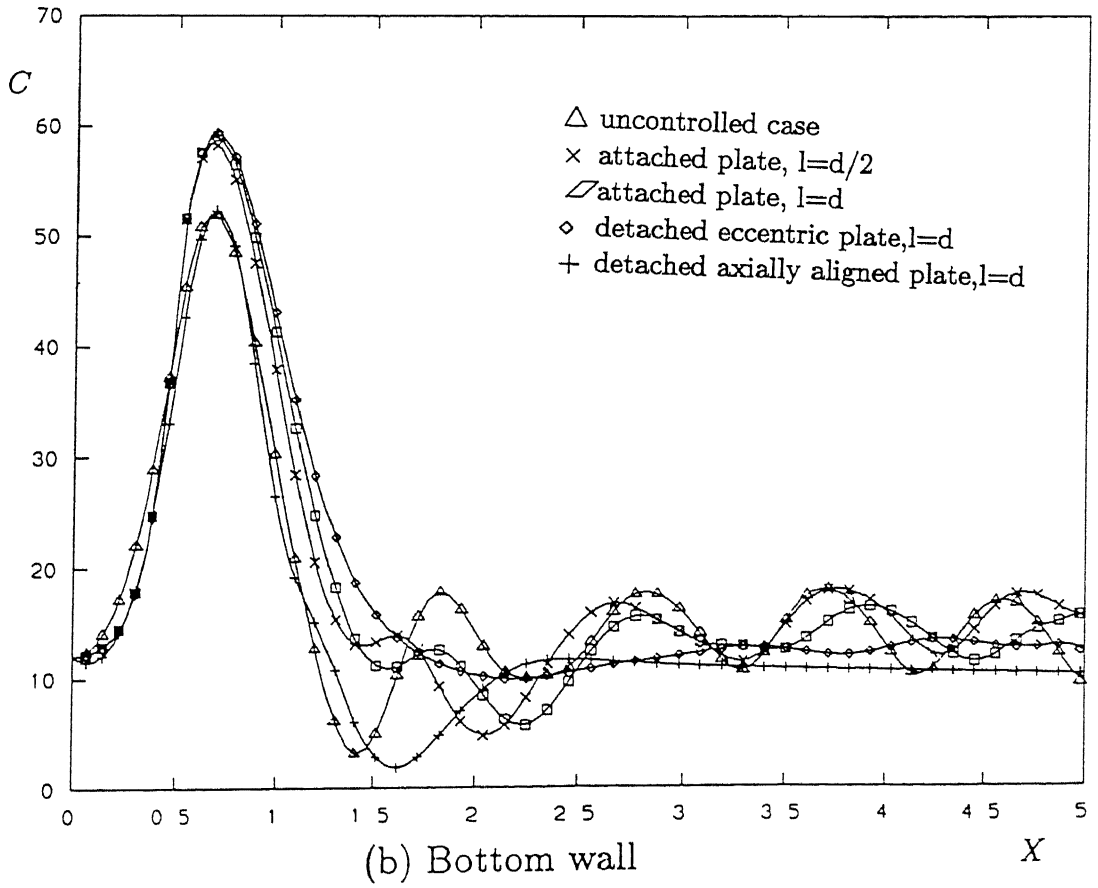

(b) Bottom wall

Figure 3.11: Skin friction distribution on the walls

with change in magnitude.

3.3 Control of Vortex Shedding Using Suction and Blowing

Use of a splitter plate is discussed in the previous section to control the vortex shedding from a circular cylinder. Use of thin plates in the flow field may not be possible in some cases. Structures used in aircraft can be cited as one of such example. Here, control of vortex shedding should be attained by some other means. Ignoring body forces, the momentum equation in the main flow direction can be written as

$$\rho\left(\frac{\partial u}{\partial t} + u\frac{\partial u}{\partial x} + v\frac{\partial u}{\partial y}\right) + \frac{\partial p}{\partial x} = \mu\frac{\partial^2 u}{\partial y^2} \tag{3.1}$$

Where ρ is the density, u, and v are the velocities in the flow and normal directions, p is the pressure and x, y are the spatial coordinates. The right-hand side term of equation (3.1) represents the flux of vorticity at the surface. Any term on the left hand side of equation (3.1) can affect the sign and magnitude of the vorticity flux and hence the flow. Wall injection and suction alters the left hand side, mainly through the pressure gradient. It is not possible to say what quantity of injection or suction will help in avoiding the vortex shedding as the governing equation is nonlinear and the parameters controlling the flow are many. Control using injection and suction has been attempted by many researchers. To do it actively, a signal which controls the quantity of injection or suction has to be fed back through a control loop. Location of the sensor in the flow field, deciding the parameter to be monitored, and the control law which governs the quantity of injection and suction, are difficult to determine. Gunzburger and Lee(1996) have explained the difficulties in choosing the above mentioned parameters. In this study we chose three orifices on the downstream side of the cylinder. The location of orifices is shown in Figure 3.12 and its

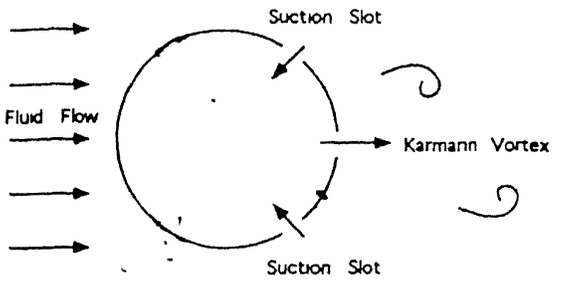

Figure 3.12: Location of orifices

size is $3\pi/40$. An effort is made to keep the mass of fluid sucked and injected as same which avoids the need of keeping a separate source to supply the fluid. Fluid is sucked through the orifices centered at $\pi \pm \pi/4$, blown from orifice centered at π. Computation have been carried out with different suction/injection rates. (hereafter it will be called control parameter, control parameter of value one means that the the rate of suction and blowing is approximately $1/20^{th}$ of the main flow flow rate) times the length of orifice.

When the control parameter is 0.5, the St increases to 0.3558 from 0.3450, and the asymmetry in the flow remains (Figure 3.13). The vortex generation is pushed downstream. Vector profiles and isothermal lines (Figures 3.13(a), 3.13(b)) shows that the unsteadyness in the downstream is still existing.

Increasing the control parameter from 0.5 to 1, St increases to 0.3616. But the normal velocity signal (Figure 3.14(a)) shows that the amplitude of fluctuation of velocity in the downstream reduces considerably. From Figure 3.14(b) it is evident that the formation of vortices is moved away from the cylinder. This is because of the strong injecting velocity in the flow direction from the cylinder base. Due to suction, the pressure near the suction orifices is small compared with that of the injection orifice region. This pressure difference results in the flow from, the downstream region towards the suction orifices. Due to this, there are weak vortices formed near the suction orifices (Figure 3.14(b)). Figure 3.14(c) shows the isothermal lines. It is observed that the uniform distribution in the temperature is maintained up to some point in the downstream after which the effect of flow oscillation

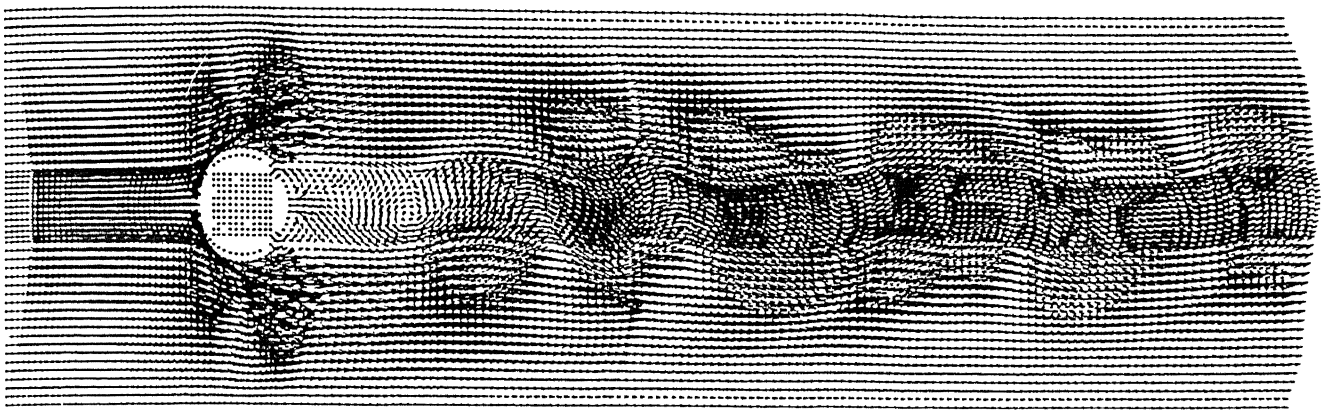

(a) Velocity profile

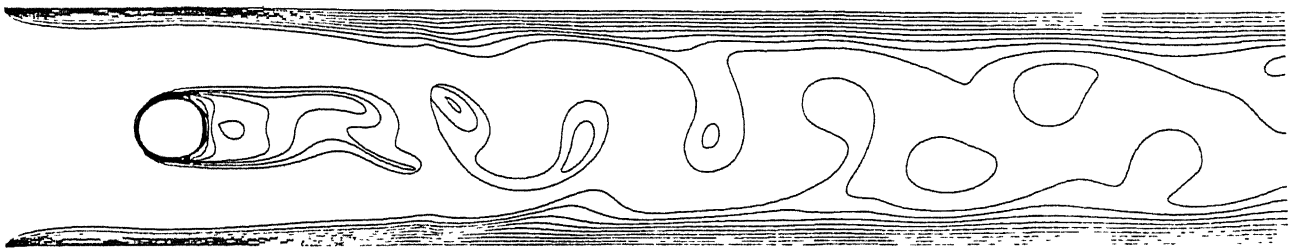

(b) Isotherms

Figure 3.13: Velocity profiles and isothermal lines for control = 0.5

is seen. This point is moved downstream compared with the uncontrolled case.

With increasing the control parameter to 2, St increases significantly to 0.463. But the fluctuation in the amplitude of normal velocity is reduced (Figure 3.15(a)). The velocity profiles and streamlines (Figures 3.15(b), 3.15(c)) shows there are secondary vortices which are formed near the suction orifices as discussed above. But because of large pressure difference between suction and injection orifices, the secondary vortices are relatively strong. This results in almost parallel vortex generation from the top and bottom of the cylinder and thus the increase in St. The temperature distribution (Figure 3.15(d)) in the wake is also changed considerably. The fluctuation of temperature near the walls is almost eliminated in this case compared with the uncontrolled one. The thermal energy which is convected from the cylinder is also restricted in the narrow region of width equal to the diameter approximately which is over the hole region for the earlier cases.

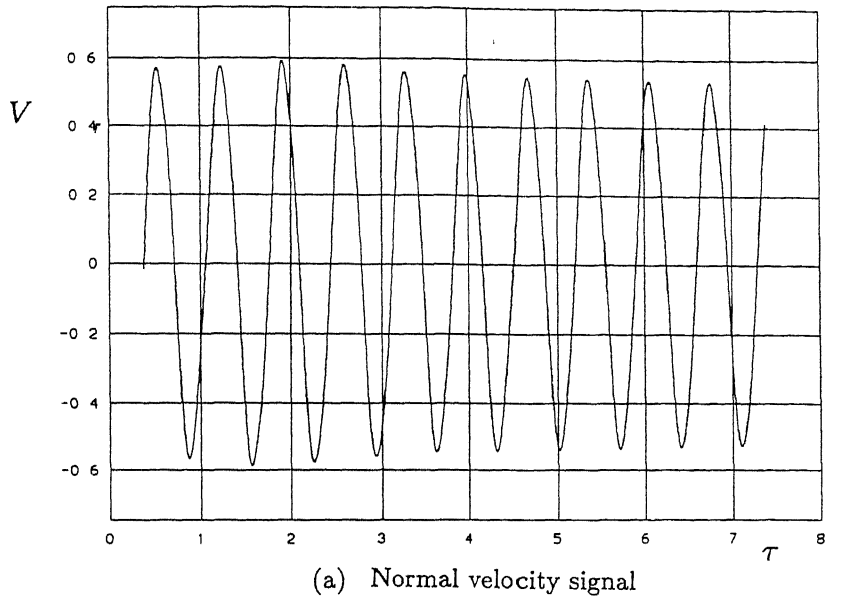

(a) Normal velocity signal

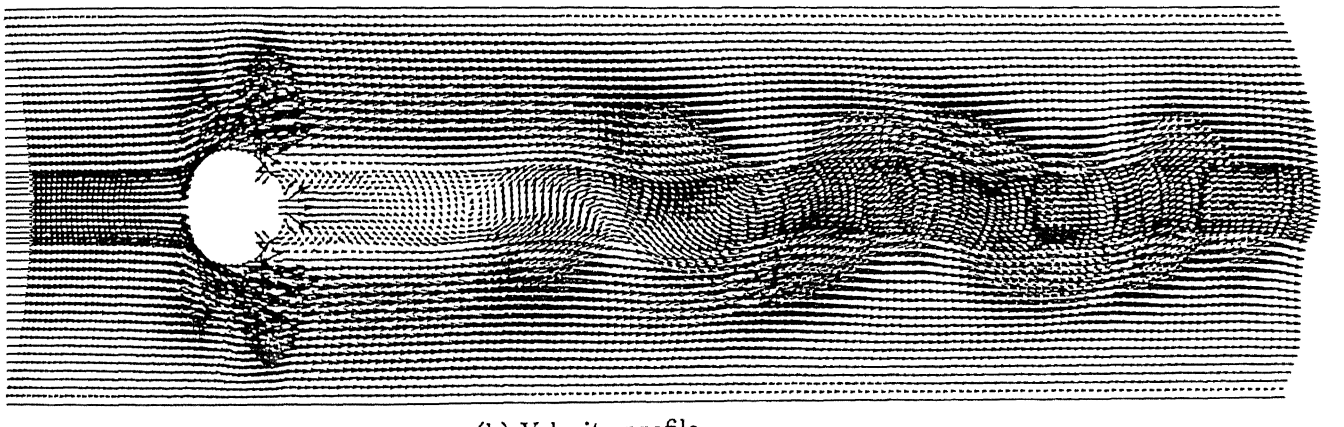

(b) Velocity profile

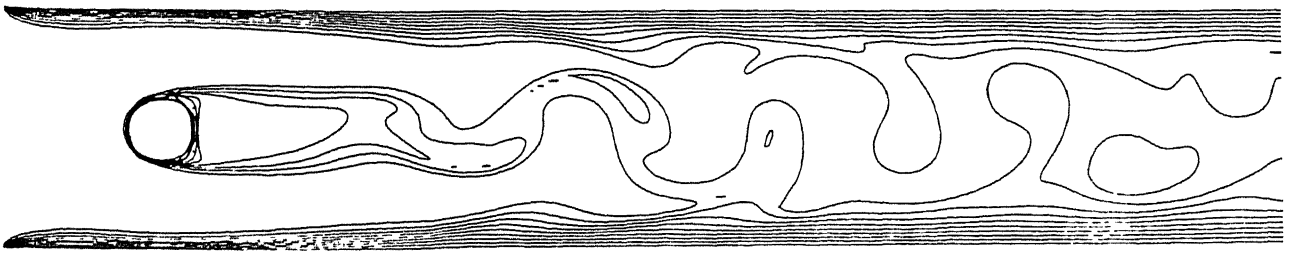

(c) Isotherms

Figure 3.14: Velocity signal, velocity, streamline and isothermal plot for control =1.0

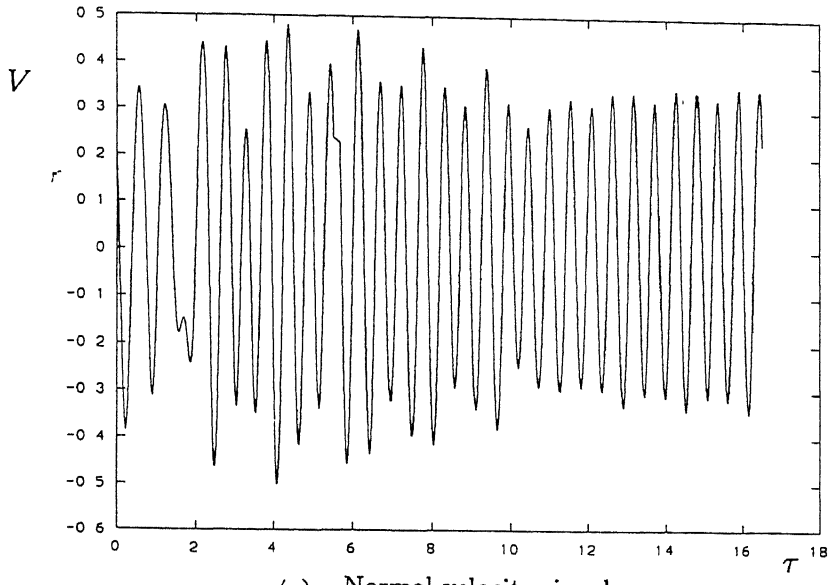

(a) Normal velocity signal

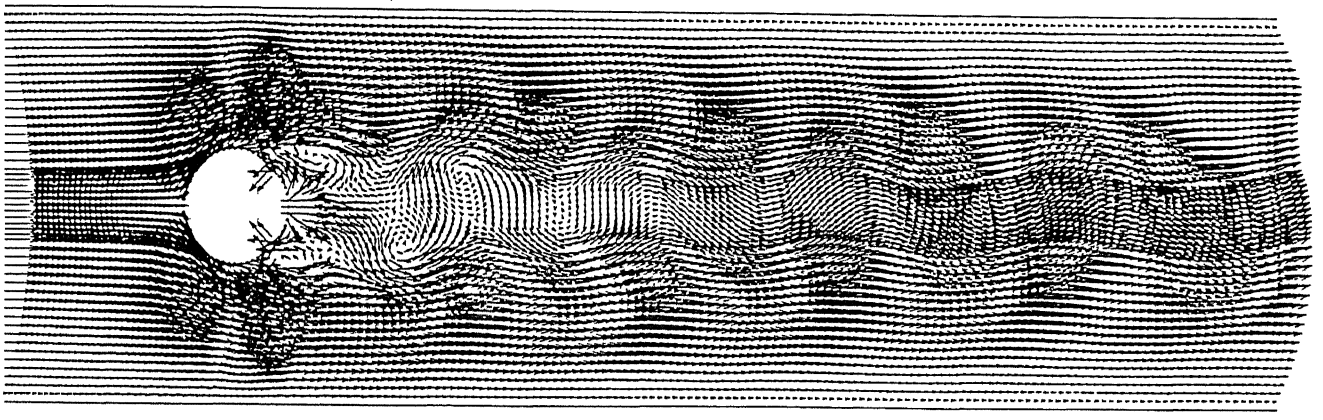

(b) Velocity profile

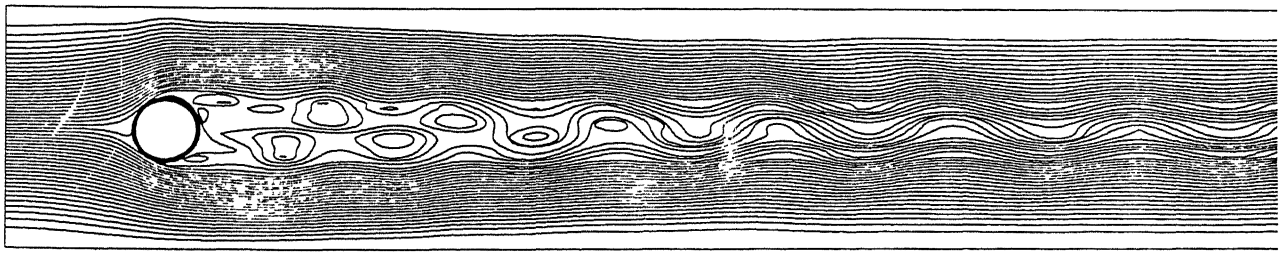

(c) Streamlines

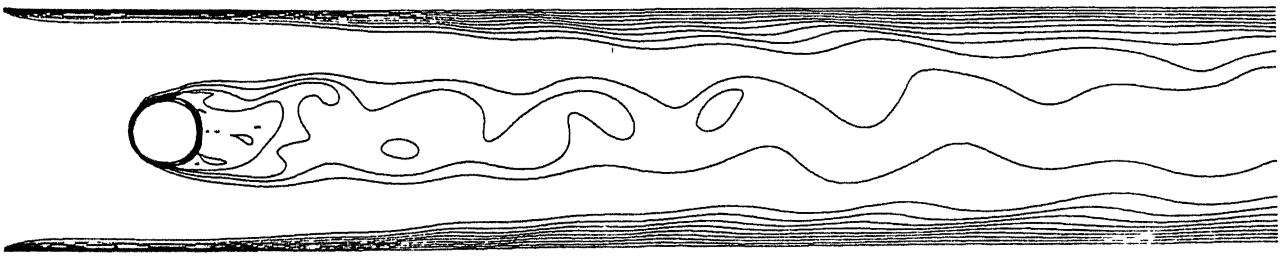

(d) Isotherms

Figure 3.15: Velocity signal, velocity, streamline and isothermal plot for control =2.0

Lastly when the control parameter is increased further, the fluctuation in the normal velocity increased more than the uncontrolled case (Fig. 3.16(a)). Now there is slight decrease in the St (0.4113) but still more than that for the uncontrolled case. It is observed from Figures 3.16(b), and 3.16(c) that unlike earlier cases, the main vortices are very close to the cylinder and are of strong magnitude. This makes the main and secondary vortices interact and thus the change in trend takes place. Shedding takes place alternatively and it results in more fluctuation of velocity in the downstream. Isothermal plot (Figure 3.16(d)) supports the above observation as the isotherms around the cylinder moves up to the walls as the flow moves downstream which implies better mixing in the downstream.

It is observed from the above studies that with three slots and within this control parameter range, it is not possible to reduce the vortex shedding. It can only be increased. When the control parameter is 2, there is change in the effect of injection and blowing. It should be mentioned that below this value, there is increase in St and the velocity fluctuation is reduced; the vortices are not strong and this is the reason, the fluctuation is less However, a control parameter value of 2, the secondary vortices which are formed near the suction orifices are strong and resulting in higher fluctuation downstream. However the St is reduced.

Since the flow is not steady, the pressure at the base of the cylinder varies with time. Thus having a constant suction/blowing may not result in complete suppression of vortex shedding. It is also evident that the pressure variation in the downstream of the cylinder it is related to base side pressure. Having decided to take pressure as the feedback parameter, the above observation helps in deciding the location of the sensor. Two sensors at a distance of two times the diameter from the cylinder base are placed one each on the cylinder walls.

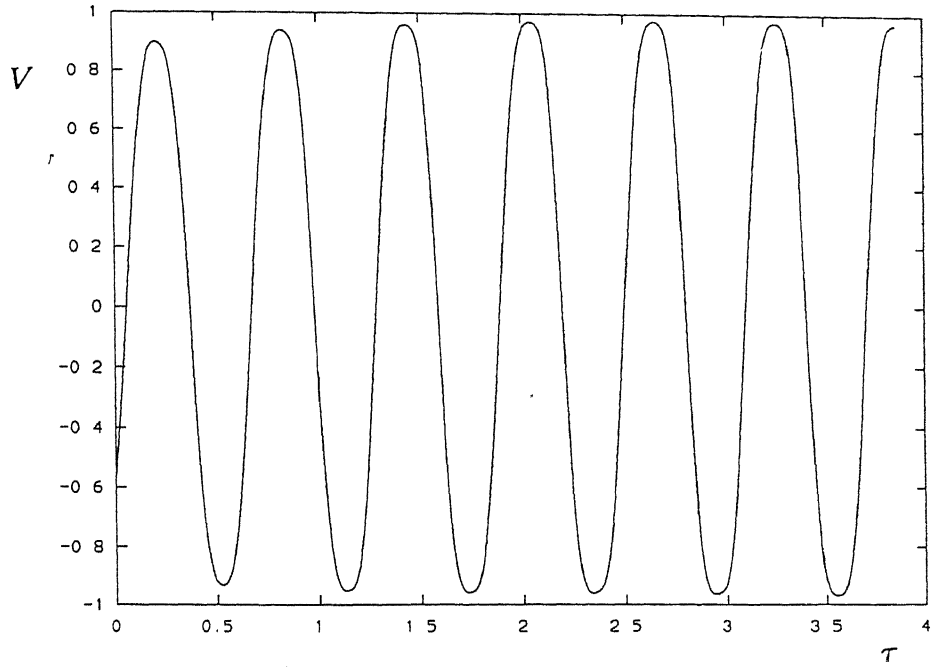

(a) Normal velocity signal

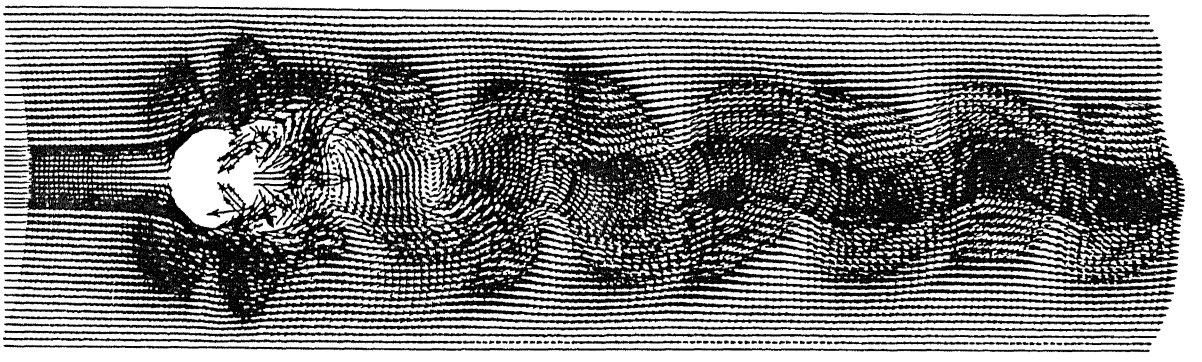

(b) Velocity profile

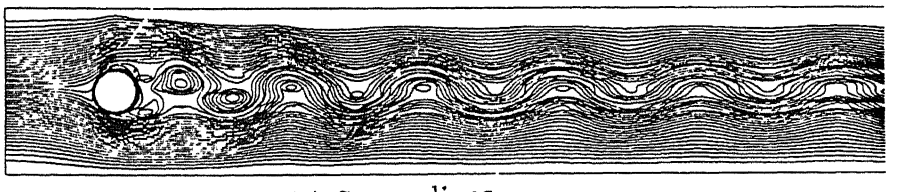

(c) Streamlines

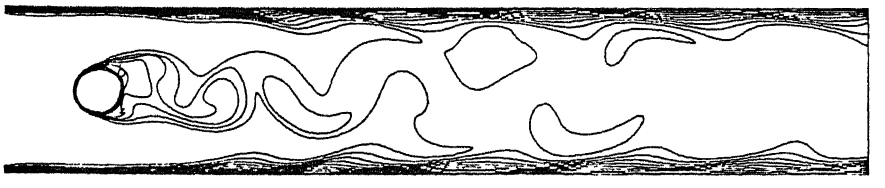

(d) Isotherms

Figure 3.16: Velocity signal, velocity, streamline and isothermal plot for control =3.0

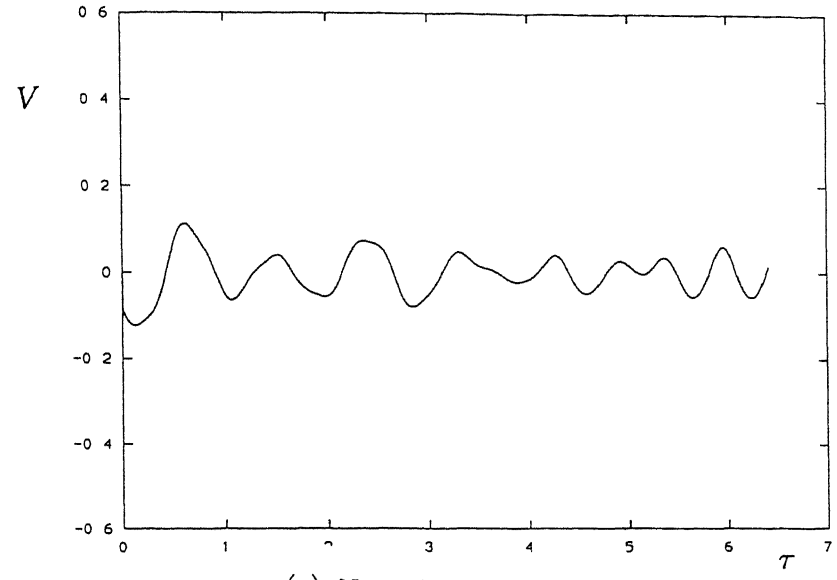

(a) Normal velocity signal

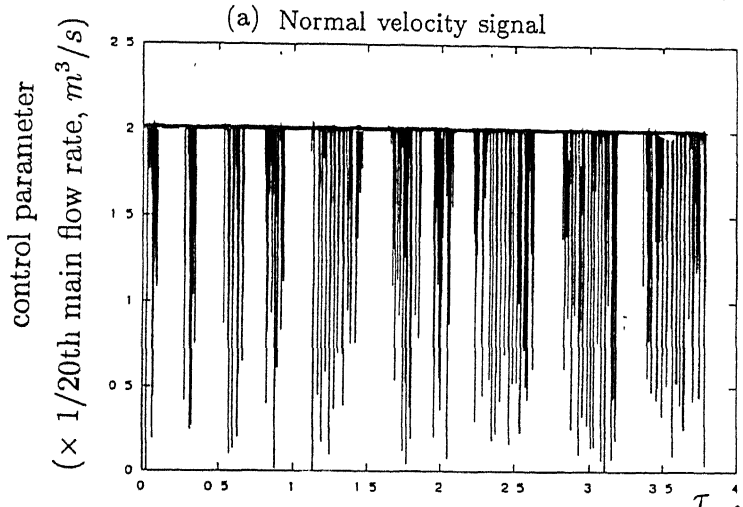

(b) Time variation of suction/blowing quantity

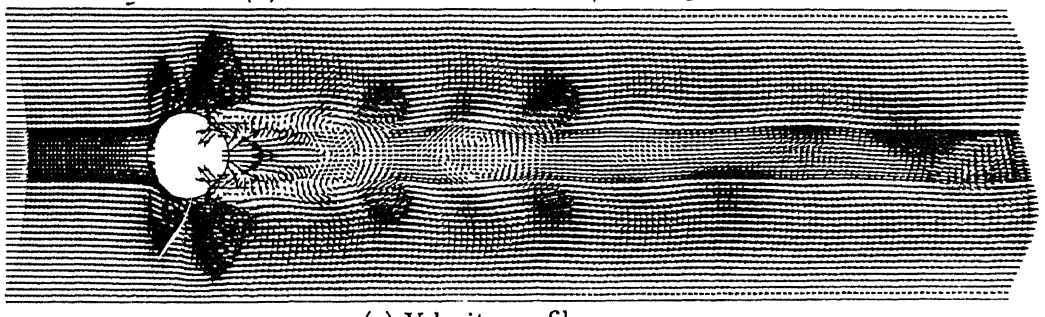

(c) Velocity profile

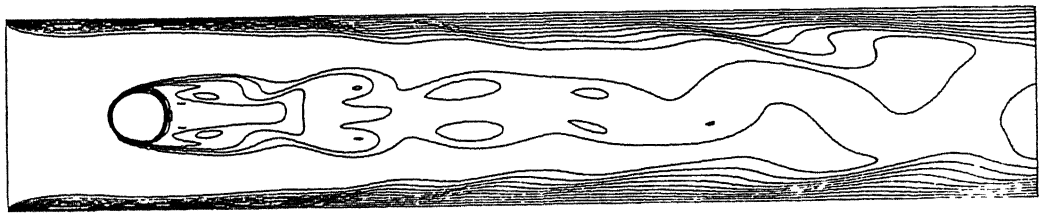

(d) Isotherms

Figure 3.17: Velocity signal, velocity, streamline and isothermal plot with active control

The difference in pressure is used as the feedback signal in the feedback law given below (Gunzburger and Lee(1996)).

$$u_i \cdot \hat{n} = \min \{\alpha \mid \delta p \mid, \beta\} \tag{3.2}$$

where u_i is the velocity of flow in x,y directions, $\hat{n}$ is the unit outward normal, α is the constant, δp is the measured pressure difference and β is the maximum limit of the control parameter. Here again to keep the flow rate balanced, total quantity sucked from the two orifices are made equal to the amount of injection. From the above study, we decided to keep the maximum of control parameter value as 2. The value of α is chosen to keep the the control parameter as close as possible to the value 2. By studying δp, it is found that $\alpha = 25$ will serve this purpose. Figure 3.17(a) gives the velocity fluctuation in the downstream (at the same location of previous study) and it can be seen that the fluctuation is reduced drastically with active control. The change in the control parameter with time is given in Figure 3.17(b). Figures 3.17(c) and 3.17(d) show the velocity field and isothermal lines with active control. This small fluctuation in the velocity implies that the fluctuation in the lift and drag forces are reduced to a great extent.

3.4 Closure

The effect of thermal buoyancy on the flow and heat transfer parameters are studied for Re=200. It is found that the effect of thermal buoyancy is significant near the walls. But it does not change the flow dramatically. Increase in thermal buoyancy increases the heat transfer from the bottom wall and reduces it from the top wall. On the cylinder surface there is not much effect except near the separated region where there is slight increase in heat transfer. Effect of the thermal buoyancy on St is almost negligible. Numerical experiments have been carried out for different configuration of splitter plate placed in the

downstream of the cylinder. It is found that for the same length of plate, keeping the plate detached from the cylinder controls vortex shedding better than placing it attached to the cylinder. With the plate length equal to the diameter of the cylinder placed axially detached from the cylinder at a distance of one diameter eliminates vortex shedding completely. Next, the results of using suction and blowing from the cylinder to control the vortex shedding were discussed. It is found that with constant suction and blowing it is not possible to suppress the shedding. Feedback control with the same configuration and using a simple feedback law, reduction in the size of oscillation of the normal velocity component is achieved.

Chapter 4

Conclusion

Use of circular tubes in heat exchangers and the complexity in understanding the flow physics motivates us to study the flow and heat transfer characteristics past a circular cylinder. The effect of thermal buoyancy force on the fluid flow and heat transfer, and control of vortex shedding from the cylinder placed in a horizontal channel are studied numerically. The equations governing the fluid flow for a two dimensional laminar flow are derived in its integral form. A explicit control volume formulation based on EXTRA-FLAG (A. Mukhopadhyay; 1993) is used to solve the equations.

- For the flow Reynolds number of 200, the effect of thermal buoyancy force on forced flow is investigated. It is found that the effect of thermal buoyancy is significant near the walls. But it does not effect the main flow. Increase in thermal buoyancy increases the heat transfer from the bottom plate and reduces it from the top plate. On the cylinder surface, only in the separated region there is slight increase in heat transfer. Effect of the thermal buoyancy on the frequency of vortex shedding is almost negligible.

- Use of splitter plate attached to the cylinder results in change in Strouhal number. It is observed that it is not possible to suppress the shedding completely using the

splitter plate smaller than one diameter length. Placing a plate of length equal to one diameter detached from the cylinder, at a distance equal to one diameter, completely suppresses vortex shedding. When moved slightly eccentric from the above position, shedding of weak vortices is observed.

- Numerical experiments have been carried out with suction and injection of fluid from the cylinder wall. It is observed that with constant quantity of suction and blowing, it is not possible to reduce the vortex shedding frequency. Active control of the flow shows that great reduction in the fluctuation of velocity in the wake of cylinder is possible with very simple feed back law. But the feed back law used is not optimal. Designing a optimal feed back law may help in suppressing the vortex shedding completely.

ABSTRACT

The effect of thermal buoyancy force on fluid flow and heat transfer, and control of vortex shedding from a circular cylinder placed in a horizontal channel are studied numerically. An explicit control volume formulation is used to solve the governing mass, momentum and energy equations. Change in skin friction and the heat transfer rate from the channel walls and cylinder surface are observed due to thermal buoyancy force. Modification in the Strouhal number is not much which implies the flow is not altered significantly by the thermal buoyancy force. Control of vortex shedding from the circular cylinder has been attempted by (i) placing the splitter plate in the downstream and (ii) suction and injection of fluid from the cylinder surface. Different combinations of length and location of splitter plate are studied. Splitter plate placed axially away from the cylinder, with length equal to one diameter of the cylinder, suppresses vortex shedding completely. Studies with constant quantity of suction and blowing are discussed. From the observations made, and using a simple feed back law, active control of vortex shedding is attempted. Results show there is substantial reduction in the oscillation of normal velocity in the downstream.

References

[1] Biswas G., Laschefski H., Mitra N., and Flebig M. Numerical investigation of mixed convection heat transfer in a horizontal channel with a built-in square cylinder. *Numerical Heat Transfer*, pages 173 – 188, 1990. Vol. 18, Part A.

[2] Blevins R.D. The effect of sound on vortex shedding from cylinder. *J. Fluid Mech.*, pages 217 – 237, 1985. Vol. 161.

[3] Chen C.H. and Weng F.B. Heat transfer for incompressible and compressible fluid flows over a heated cylinder. *Numerical Heat Transfer*, pages 325 – 342, 1990. Vol. 18, Part A.

[4] Cheng K.C. and Hwang G.J. Numerical simulation for combined free and forced laminar convection in horizontal rectangular channels. *J. Heat Transfer*, pages 59 – 66, 1969. Vol. 91.

[5] Coutanceau M. and Bouard R. Experimantal determination of the main features of the viscous flow in the wake of circular cylinder in uniform translation. *J. Fluid Mech.*, pages 257 – 272, 1977. Vol.72, Part 2.

[6] Frick C.W. and McCullough. Tests of a heated low drag airfoil. 1942. NACA ARR, December.

[7] Gad-el-hak M. Flow control. *Appl. Mech. Rev.*, pages 261 – 293, 1989. Vol. 42, no 10.

[8] Gad-el-hak M. Modern developments in flow control. *Appl. Mech. Rev.*, pages 365 – 379, 1996. Vol. 49, no 7.

[9] Grinstein F.F., Boris J.P., and Griffin O.M. Passive pressure-drag control in a plane wake. *AIAA Journal*, pages 1436 – 1442, 1991. Vol.29, no. 9.

[10] Gunzburger M. D. and Lee H. C. Feedback control of karman vortex shedding. *Transaction of ASME*, pages 828 – 835, 1996. Vol.63.

[11] Harlow F.H. and Welch J.E. Numerical calcualtion of time-dependent viscous incompressible flow of fluid with free surface. *The Phys. Fluids*, pages 2182 – 2188, 1965. Vol. 8.

[12] Harlow F.H. and Amsden A.A. The smac method: A numerical technique for calculating incompressible fluid flows. 1970. Los Almos, Scientific Lab. Rept LA 4370.

[13] Incropera F.P. and Schutt J.A. Numerical simulation of laminar mixed convection in the entrance region of horizontal rectangular ducts. *Numerical Heat Transfer*, pages 707 – 729, 1985. Vol. 8.

[14] Incropera F.P., Knox A.L., and Maughan J.R. Mixed convection flow and heat transfer in the entry region of rectangular duct. *J. Heat Transfer*, pages 434 - 439, 1987. Vol. 109.

[15] Kown K. and Choi H. Control of laminar vortex shedding behind a circular cylinder using a splitter plate. *Phys. of Fluids*, pages 479 - 486, 1996.

[16] Liepmann H.W. and Fila G.H. Investigations of effects of surface temperature and single roughness elements on boundary layer transition. 1947. NACA report no 890.

[17] Majumdar S., Rodi W., and Vanka S.P. On the use of non-staggered pressure-velocity arrangement for numerical solution of incompressible flows. 1987. Technical report SFB 210/T/35 November.

[18] Mukhopadhyay A., Sundararajan T., and Biswas G. An explicit transient algorithm for predicting incompressible viscous flows in arbitrary geometry. *Int. J. Numer. Meth. fluids*, pages 975 - 993, 1993. Vol. 17.

[19] Ongoren A. and Rockwell D. Flow structure from an oscillating cylinder part i mechanisms of the shift and recovery in the near wake. *J. Fluid Mech.*, pages 197 - 223, 1988. Vol. 191.

[20] Patankar S.V., Ramadhani S., and Sparrow E.M. Effect of circumferentially nonuniform heating on laminar combined convection in a horizontal tube. *J. Heat Transfer*, pages 63 - 70, 1978. Vol. 100.

[21] Patankar S. V. Numerical heat transfer and fluid flow. 1980. Hemisphere, Washington, D. C.,.

[22] Patankar S.V. A calculation procedure for two dimensional elliptic situations. *Numerical Heat Transfer*, pages 409 - 425, 1981. Vol. 4.

[23] Patnaik B.S.V.P., Seetharamu K.N., and Narayana P.A.A. Simulation of laminar confined flow past a circular cylinder with integral wake splitter involving heat transfer. *Int. J. Num. Meth. Heat Fluid Flow*, pages 65 - 81, 1996. Vol.6 no. 4.

[24] Peyret R. and Taylor T.D. Computational methods for fluid flow. 1983. In Springer Series in Computational Physics, Springer-Verlag, New york.

[25] Raithby G.D. and Wolfstein M. Upstream-weighted schemes and their application to elliptic problems involving fluid flow. *Comput. Fluids*, pages 191 - 206, 1974. Vol. 2.

[26] Shaira F.H., Grove A.S., Petersen E.E., and Acrivos A. The effect of confining walls on the stability of the steady wake behind a circular cylinder. *J. Fluid Mech.*, pages 546 - 550, 1963. Vol. 17.

[27] Strykowski P.J. and Srinivasan K.R. On the formation and suppression of vortex shedding at low reynolds numbers. *J. Fluid Mech.*, pages 71 - 107, 1990. Vol. 218.

[28] Wang M. and Georgiadis J.G. Conjugate force convection in crossflow over a cylinder array with volumetric heating. *Int. J. Heat Mass Transfer*, pages 1351 - 1361, 1996. Vol. 39, No. 7.